

(NASA-TM-78489) AN EXPERIMENTAL
INVESTIGATION OF HINGELESS HELICOPTER
ROTOR-BODY STABILITY IN HOVER (NASA) 49 p
HC A03/MF A01

CSCI 02A

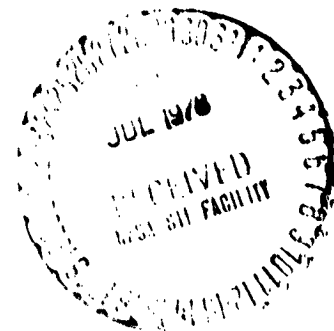
N78-29044

Unclass
25132

G3/01

An Experimental Investigation of Hingeless Helicopter Rotor-Body Stability in Hover

William G. Bousman



NASA
National Aeronautics and
Space Administration

United States Army
Aviation Research
and Development
Command



An Experimental Investigation of Hingeless Helicopter Rotor-Body Stability in Hover

William G. Bousman, Aeromechanics Laboratory
AVRADCOM Research and Technology Laboratories
Ames Research Center, Moffett Field, California



National Aeronautics and
Space Administration

Ames Research Center
Moffett Field, California 94035

United States Army
Aviation Research and
Development Command
St. Louis, Missouri 63166



AN EXPERIMENTAL INVESTIGATION OF HINGELESS
HELICOPTER ROTOR-BODY STABILITY IN HOVER

William G. Bousman

Ames Research Center
and
Aeromechanics Laboratory
AVRADCOM Research and Technology Laboratories

SUMMARY

Model tests of a 1.62-m diameter rotor were performed to investigate the aeromechanical stability of coupled rotor-body systems in hover. Experimental measurements were made of modal frequencies and damping over a wide range of rotor speeds. Good data were obtained for the frequencies of the rotor lead-lag regressing, body pitch and body roll mode, and the damping of the lead-lag regressing mode. The quality of the damping measurements of the body modes was poor due to nonlinear damping in the gimbal ball bearings. Simulated vacuum testing was performed using substitute blades of tantalum that reduced the effective Lock number to 0.2% of the model scale value while keeping the blade inertia constant. The experimental data were compared with theoretical predictions, and the correlation was in general very good.

INTRODUCTION

The body degrees of freedom of a helicopter exert a profound influence on the stability of the coupled rotor-body system for configurations whose lead-lag frequency is less than the rotor speed (soft inplane). For articulated rotors the coupling of the rotor and body inertially can result in a strong instability termed ground resonance. This purely mechanical instability is now well understood (ref. 1); however, in the case of hingeless rotors substantial aerodynamic and structural couplings may arise and the problem of aeromechanical stability is considerably more complex (ref. 2).

A number of detailed theoretical models have been developed to investigate the aeromechanical stability of soft inplane hingeless rotors (refs. 3-5), with the specific purpose of providing the analytical tools to support the design of a soft inplane hingeless rotor helicopter. In the case of Boeing Vertol a number of experiments have been performed in addition with small-scale helicopter models to verify their design concepts, and in the process validate their theoretical model (refs. 6,7). More recently, Ormiston has described a simplified theoretical model of a coupled rotor-body system (ref. 2); this model is particularly useful as a tool for obtaining a fundamental understanding of the factors that affect the aeromechanical stability of hingeless rotor helicopters. The present experiment has been designed to use a simplified experimental model to investigate the

aeromechanical stability of coupled rotor-body system in a manner analogous to that of reference 2, and in the process to develop a body of experimental data that is suitable for the validation of analytical models of coupled rotor-body stability. The development and examination of appropriate test techniques for coupled rotor-body testing are an integral part of the experiment design as well.

The testing of model rotors or helicopters can be broken down into the categories of: (1) exploratory testing of new concepts; (2) development testing of a new design; and (3) research model testing (ref. 8). The present experiment is in the last category, and it is important to distinguish that the experiment has been designed to match the theoretical model as closely as possible rather than any particular helicopter. The reason for this effort is to insure that in the validation process of a theoretical model, that any difference between the theoretical prediction and the experimental data reveal the limitations of the theoretical model, and not the experimental modeling process.

The design of the experiment is discussed first; the model used is then described, including the excitation system and instrumentation. The techniques used to excite the various rotor-body modes and the methods of obtaining damping and frequency are discussed. The experimental results are shown and compared with theoretical predictions of the analysis described in reference 9. Conclusions are offered with respect to the results of the experiment, and the worth of the experimental design.

SYMBOLS

A	flexure cross-sectional area, cm^2
a	lift curve slope
b	number of blades
c	blade cord, cm
c_{d_0}	profile drag coefficient
D	bearing damping, N-cm
E	Young's modulus, N/cm^2
e	hinge offset, cm
f_B	friction force in ball bearings, N
G	shear modulus, N/cm^2
g	gravitational acceleration, cm/sec^2

h	distance from plane formed by gimbal axes to rotor plane
I	blade inertia, $g\text{-m}^2$
I_c	flexure chordwise area moment of inertia, cm^4
I_f	flexure flapwise area moment of inertia, cm^4
I_α	blade pitching moment of inertia, $g\text{-m}^2$
I_0	body inertia about pitch axis, $g\text{-m}^2$
I_ϕ	body inertia about roll axis, $g\text{-m}^2$
J	flexure polar area moment of inertia, cm^4
J_r	rotor polar moment of inertia, $g\text{-m}^2$
K	body stiffness, N-cm/rad
k_z	vertical body spring, N/cm
L	blade length from flexure tip, cm
ℓ	flexure length, cm
ℓ_x	longitudinal spacing of vertical body springs, cm
ℓ_y	lateral spacing of vertical body springs, cm
m_B	body mass, g
m_b	blade mass, g
m_h	rotor mass, g
n_B	number of balls in ball bearing
p	rotating flap frequency, Hz
R	blade radius, cm
r_B	radius to application of bearing damping force, cm
x_b	blade spanwise mass centroid referenced to flexure tip made dimensionless by blade length L
x_c	blade chordwise mass centroid referenced to quarter chord made dimensionless by blade chord c
x_{cn}	blade spanwise mass centroid referenced to centerline, cm
x_{co}	blade root cutout, cm

γ_d	Lock number including effect of profile drag coefficient
ζ_{\cos}	rotor lead-lag cyclic coordinate, deg
ζ_{local}	local damping coefficient
ζ_{\sin}	rotor lead-lag cyclic coordinate, deg.
η_{ζ}	blade damping, percent critical
$\eta_{\phi x}$	body roll damping, percent critical
$\eta_{\phi y}$	body pitch damping, percent critical
θ	body pitch angle, rad
θ_b	blade pitch angle, deg
θ_i	peak magnitude of body pitch angle, deg
ρ	density of air, g/cm ³
ρ_d	density of uniform blade, g/cm ³
σ	rotor solidity
σ	modal damping exponent, sec ⁻¹
Ω	rotor speed, rpm
Ω_0	nominal rotor speed, sec ⁻¹
ω	modal frequency, Hz
ω_{β}	flapping mode frequency, Hz
ω_{ζ}	lead-lag mode frequency, Hz
ω_{θ}	body pitch mode frequency, Hz
ω_{ϕ}	body roll mode frequency, Hz

Subscript:

()₀ nonrotating conditions (except as noted for Ω_0)

EXPERIMENT DESCRIPTION

Experimental Design

The primary objective of the present experiment is to provide a body of experimental data that can be used to validate theoretical models for the prediction of coupled rotor-body aeromechanical stability. To obtain this goal the experimental design requires that: (1) the basis for comparison between theory and experiment must provide a rigorous test of the theoretical model; (2) the data obtained must be extensive enough to provide a varied test of the theoretical model; and (3) the experimental model must simulate the theoretical model as closely as possible.

The basis of comparison used for the present experiment is the frequency and damping of the flap and lead-lag regressing modes, and the body pitch and roll modes. These are examined over a range of rotor speeds that provide nondimensional lead-lag frequencies from stiff inplane to soft inplane. Additional variation is provided by changes in blade collective pitch angle, body stiffness, and Lock number.

The model design is based on the simplified theoretical model used in reference 2. Specifically, the blades have been designed to be very stiff, with most of the flexibility concentrated in root flexures. This provides an experimental approximation of the centrally-hinged, rigid blade with spring restraint that is used in the theoretical model. As the blade torsional degree of freedom is not included in the theoretical model, the blade and root section of the experimental model are designed to be torsionally very stiff. The model is mounted on a gimbal frame and bearings and in this way simulates purely pitch and roll body motions.

Simulated Vacuum Testing

It is highly desirable in the theoretical validation process to obtain experimental data with aerodynamic effects eliminated, but inertial and structural terms unchanged. This is especially useful in the case of hingeless rotor aeromechanical stability where the effects of aerodynamics significantly alter the behavior of coupled rotor-body instabilities of the ground resonance type. Testing in a vacuum chamber can be both difficult and expensive. However, the effects of testing in a vacuum may be simulated by reducing the Lock number of the rotor. Defining Lock number in the form:

$$\gamma_d = \frac{\rho a c R^4}{I} \left(1 + \frac{c_{d_0}}{a} \right)$$

where the conventional definition has been modified to include the effect of the blade profile drag coefficient, c_{d_0} . In vacuum testing the Lock number

is zero because the density of air is zero; however, there are other ways in which Lock number may be reduced. The particular strategy used in this experiment was to make a blade of circular cross section and in this way reduce the lift curve slope to zero. This would not be a satisfactory solution if blade flexibility were important to the problem, but in the present case it is not. If a uniform cylindrical rod is assumed, then the expression for Lock number becomes

$$\gamma_d = \frac{12\rho_d c_{d0}}{\pi} \left(\frac{R}{\rho_d c} \right)$$

where ρ_d is the density of the blade material. To further reduce Lock number it is clear that the radius must be reduced, or blade chord or density increased. The problem is constrained by the need to maintain the same blade inertia, that is

$$\rho_d c^2 R^3 = \frac{12I}{\pi}$$

However, the rotor mass will not stay constant but increase as

$$m_h = \frac{9I}{R^2}$$

as blade radius is reduced. The best choice then is to build the rod of as dense a material as is feasible, and select a radius that does not cause an excessive increase in rotor mass and body inertia, or effective hinge offset. Tantalum is the best design choice, being denser than lead and with strength characteristics of steel. A radius of about 38 cm was selected for the present experiment; the normal blade radius is 81 cm. The resulting value of Lock number is approximately 0.2% of the aerodynamic blade value.

Model Description

The model used in this experiment is a three-bladed, 1.62-m diameter rotor mounted to a body that is supported by a gimbal frame and stand that allow pitch and roll freedom. A two-view drawing that illustrates the major features of the model and stand is shown in figure 1. A photograph of the model as tested is shown in figure 2. The rotor and hub are mounted on a static mast that bolts directly to the transmission housing. The rotor is driven by two 4.5-kW electric motors through a 7.5:1 reduction transmission and a drive shaft internal to the static mast. The model is supported at either end by ball bearings that encircle the motor housing and provide the body roll freedom. The roll ball bearings are mounted in the gimbal frame which in turn is supported by a set of pitch ball bearings that mount to the rigid stand. Additional stiffening is provided the stand with tie-down cables.

The body frequencies are determined by cantilever beam springs, two springs for pitch and one spring for roll. The frequency can be adjusted by a slider on the cantilever beam spring that shortens the working length of the beam. Roll or pitching motion of the gimbal may also be locked out with a set of locking screws.

A snubbing mechanism is located in the stand directly below the model, and is capable of locking out body motion. The snubber may be actuated either by an electric motor or by releasing a compressed spring internal to the mechanism. In the latter case the model is snubbed or locked out in approximately a 0.1 sec. Under normal conditions the model is snubbed by the operator upon observing unstable motions. However, a control circuit is included that automatically releases the compressed spring and snubs the model if the lead-lag bending moment signal from the blade exceeds a preset value.

To simulate the rigid blade with spring restraint used in the theory, the rotor blades were designed to be as rigid as possible, and flexibility was concentrated in flexures at the blade root. A drawing of the root flexures in an exploded view is shown in figure 3 and a photograph in figure 4. From these figures it can be seen that the flap and lead-lag flexibility are concentrated in separate flexures. They are connected so that their centerlines are coincident. There is no blade pitch bearing, so all blade pitch angle changes are made manually by rotating the blade within its socket. The design of the root flexures is such that the torsional stiffness is quite high. The blade is a composite design using Kevlar, fiberglass, and balsa wood in its construction, as shown in figure 5. The spar is made up of unidirectional plies of Kevlar with a final 45° bias crossply to add torsional stiffness. The Kevlar spar and balsa wood aft section are enclosed in a fiberglass skin and mated with a titanium root section to make the final blade.

Although most of the flexibility is concentrated in the root flexures, the flexibility of the blade does influence the flap and lead-lag frequencies. This effect can be estimated by looking at the change in non-rotating blade frequencies as blade pitch angle is changed. This was done in reference 10 for the present blade and flexures, and the R parameter of Ormiston and Hodges (ref. 11), which relates the amount of flexibility outboard of the blade pitch bearing to the total blade flexibility, was estimated as 0.13.

The model with the stub blades made of tantalum installed is shown in figure 6. The tantalum rods are pinned into a steel grip which is bolted on to the outer section of the flap flexure. Flapping stops are included in this configuration to keep the heavier tantalum stub blades from causing excessive stress in the flap flexures when the rotor is stopped.

The model properties needed for correlation with the experimental data have either been measured on the model under nonrotating conditions or calculated from model design data. These properties and their determination are discussed in appendix A.

Model Excitation

An electromagnetic shaker was used to excite the rotor and body modes by oscillating or deflecting the model about its roll axis. The shaker was capable of model excitation down to zero frequency, and this was especially useful near resonance of the lead-lag mode with rotor speed. Figure 7 shows the shaker connection to the model. A pair of beams, bolted to the underside of the model transmission, extend outward and up to a cross piece that is held by a small, pneumatically-actuated clamp. The pneumatic clamp provides a means of holding on to the cross piece during model excitation, and by opening the clamp at the same time the excitation is stopped the model motions can decay without restraint from the shaker and its linkages. The pneumatic clamp is mounted on a linkage that passes down through supports used for alignment to a bell crank that is connected in turn to the shaker. Preload springs are included in the linkage to center the pneumatic clamp with the cross piece. A pair of opposed air cylinders are used as a secondary means of locking out model motion.

Model Instrumentation

Each blade root flexure was instrumented with a full strain gage bridge to measure lead-lag bending moment (on the lead-lag flexure), and flap and torsion bending moment (on the flap flexure). The signals were routed through the drive shaft to a 60-channel slip ring mounted in the base of the model.

Body motions were measured in two ways: first, with accelerometers mounted on the static mast just below the hub, and second, with resistive film potentiometers mounted at the pitch and roll bearing locations. Measurements of rotor speed were made with an inductive pickup from a 60-tooth gear, and an optical pickup providing a one-per-rev spike.

Instrumentation cables from the slip ring and from body measurements were combined with transmission oil lines, water cooling lines, motor power, and thermocouple wires and routed through brackets at the pitch and roll pivot points to minimize the effect of cable motion on body damping (see fig. 6).

AEROMECHANICAL STABILITY TESTING

Parameter Variation

For each test configuration, changes in rotor speed provide the means of varying the rotor characteristics over a wide range. This is illustrated in figure 8 where the uncoupled rotor progressing and regressing mode frequencies are plotted in the fixed system as a function of rotor speed. (The rotating system flap and lead-lag frequencies are shown for clarity.) At about 440 rpm the lead-lag motion is in resonance with rotor speed, that

is $\omega_L = \Omega$ in the rotating system (or $\Omega - \omega_L = 0$ in the fixed system). Lower rotor speeds are representative of stiff inplane configurations, $\omega_L > \Omega$; while higher rotor speeds are representative of soft inplane configurations, $\omega_L < \Omega$. Aeromechanical instabilities of the ground or air resonance type may occur in this latter region if a body mode frequency is proximate to the lead-lag regressing mode frequency. To investigate these instabilities the body frequencies for this experiment were selected in the range 0 - 5 Hz.

A test configuration was defined by (1) whether the tantalum stub blades or aerodynamic blades were used; (2) if both pitch and roll freedom were allowed or only roll; (3) the selected body stiffnesses; and (4) in the case of the aerodynamic blades, the blade pitch angle. The configurations tested in this experiment are listed in table 1.

TABLE 1. - EXPERIMENTAL CONFIGURATIONS TESTED

Blades	Pitch frequency, Hz	Roll frequency, Hz	Pitch angle, deg
Tantalum ↓	27.4 (Locked out) ↓	0.75	--
		1.89	
		2.60	
		4.11	
	2.58	2.55	↓
Aerodynamic ↓	27.4 (Locked out)	2.79	0.0
	2.62	2.73	0.0
	2.62	2.73	8.9

For those conditions where the pitch degree of freedom was locked out by restraining the gimbal frame, the first cantilever pitch-mode frequency of the body was about 27 Hz which places it well away from the regressing mode frequencies (fig. 8).

Modal Measurements

A rigorous test of a theoretical model requires that experimental measurements be made of those modes that have a significant effect on coupled rotor-body aeromechanical stability. In the present experiment most of the

effort was directed toward obtaining estimates of the frequency and damping of the rotor regressing modes and the body pitch and roll modes.

The rotor lead-lag regressing mode is generally the least stable mode of a coupled rotor-body system, and it is therefore desirable to observe this mode directly in the nonrotating system. To do this, the individual flexure lead-lag bending signals were transformed to fixed system coordinates using the multiblade transform of reference 12. This transform provides the multiblade cyclic coordinates, ζ_{sin} and ζ_{cos} which represent the rotor center of gravity position due to blade lead-lag motion. Both progressing and regressing modes appear in each cyclic coordinate, but because of their large difference in frequency they are easily separated by filtering. The ability to directly observe the regressing or progressing mode greatly simplified the operation of the experiment. Estimates of the modal frequency and damping were obtained by exciting the lead-lag regressing mode with the shaker. The excitation was then cut off, the model released, and frequency and damping were estimated from the transient decay. Frequency measurements were made on line with a spectrum analyzer, the resolution of the measurements being 0.08 Hz. The transient decay was also recorded on oscillograph and FM analog tape, and the multiblade cyclic coordinate was passed through a tracking filter that included a log magnitude output for analysis of both frequency and damping (ref. 13).

The flap regressing mode of the rotor is normally heavily damped due to blade aerodynamic damping, and it is therefore difficult to excite the mode or measure its frequency and damping. However, for test configurations using the tantalum stub blades there is negligible blade aerodynamic damping and the mode is readily excited. The flap regressing mode shows strong participation in both the flap cyclic coordinates and the body coordinates. The body modes also show substantial participation in both the flap cyclic and body coordinates. Modal measurements of both the flap regressing mode and body modes were therefore made in the body coordinates and separated with a tracking filter. Both flap regressing and the body roll modes were excited directly by deflecting the model in roll and releasing it. The body pitch mode was excited indirectly through gyroscopic coupling. As in the case with the lead-lag regressing mode, frequency estimates were made on line with a spectrum analyzer, and a tracking filter was used later for estimating frequency and damping from analog tape records. In general, the nonlinear damping characteristics of the gimbal bearings prevented satisfactory estimates of body or flap regressing mode damping.

TEST RESULTS

Correlation Model

The experiment was designed to match the theoretical model described in reference 2. However, the centrally-hinged blade model of reference 2 was approximated in the experimental model with an offset hinge. As a result, there is a significant frequency shift between theory and experiment

due to hinge offset. This is especially noticeable in the tantalum stub blade case where the nondimensional hinge offset is quite large due to the small blade radius. The analytical model described in reference 9, however, is well suited for correlation with the present experimental data since the torsionally stiff, root flexure configuration of the experimental model is a special case of a bearingless rotor.

The theoretical model of reference 9 assumes three or more rigid blades are attached to root flexures, each of which has three angular and three linear degrees of freedom. The blades may be constrained at their root by various pitch link geometries or, as in the present case, with no constraint. The body is assumed to be rigid with lateral, longitudinal, pitch and roll degrees of freedom. For air resonance stability the body motions are unconstrained, while for ground resonance stability the body is assumed to be mounted on springs, and the appropriate body frequencies are determined by the spring stiffness and their offset from the body reference center. For correlation with the experimental data the body translational degrees of freedom are suppressed and the body stiffness is determined by vertical springs and their distance from the mass center. Parameter values for the theoretical model (ref. 9) are identified in appendix B.

Tantalum Blades with Roll Freedom

Regressing modes. - Frequency and damping measurements were made with the tantalum stub blade configuration and the gimbal pitch degree of freedom locked out. Four different roll spring stiffnesses were used to provide a variation in body roll frequency. (Roll spring stiffness was determined by the position of the slider on the cantilever beam spring except for the lowest stiffness case, $\omega_{\phi 0} = 0.75$ Hz, where the cantilever beam spring was removed and very soft coil springs were substituted.) Measurements were made for rotor speeds from 250 to 1000 rpm, which provided nondimensional rotor lead-lag frequencies ranging from 1.7/rev to 0.7/rev. The data for these four conditions are shown in figures 9 to 12, and compared with the theoretical predictions.

Modal frequency data were obtained for the lead-lag and flap regressing modes, and the body roll mode. The modes were identified from the experimental data by the physical coordinates they appeared in and by the method of excitation used. Thus, the lead-lag regressing mode is always identified by circles, the flap regressing by triangles, and so forth. The modes predicted by the theory, however, sometimes change character as rotor speed is varied. In figure 9(a), for instance, the lowest frequency mode starts out as the body roll mode under nonrotating conditions, and as rotor speed is increased it becomes predominantly a flap regressing mode. As rotor speed is further increased, this mode couples with the lead-lag regressing mode and a modal crossover occurs where the flap regressing mode becomes predominantly lead-lag regressing, and the lead-lag regressing mode becomes predominantly flap regressing. In other cases two modes may cross without a change in character, as in figure 9(a) where the lead-lag regressing and body roll modes cross at 280 rpm. The predominant physical

character of the theoretically predicted modes is indicated in these figures by letters: ζ for lead-lag regressing, β for flap regressing, and so forth. At rotor speeds above the resonance of blade lead-lag motion and one-per-rev, that is where $\omega_r = \Omega$ or $\Omega - \omega_r = 0$, the theoretical model predicts that the lead-lag and flap regressing modes coalesce over a very narrow range in rotor speed. This coalescence is shown in an inset at 5 times scale on the modal frequency plots. The frequency coalescence is associated with a weak instability that was discussed in reference 2.

Estimates of the lead-lag regressing mode damping are also shown in figures 9 to 12. Attempts to measure the flap regressing and body roll mode damping were made, but these modes showed strong nonlinear damping behavior characteristic of the nonlinear damping of the gimbal ball bearings (see appendix A) and the attempts were abandoned. Theoretical predictions of both flap and lead-lag regressing mode damping are presented in these figures, as these modes are strongly coupled, and as rotor speed varies these two modes switch character. Where the modal damping is predominantly lead-lag or flap this is indicated on the figures with the symbols ζ or β , respectively. Because of the nonlinear character of the gimbal bearing damping, the selection of a damping value for the theoretical model is somewhat arbitrary. The effect of different levels of bearing damping was investigated by both halving and doubling the nominal value of 3%. This effect is shown for the lead-lag regressing mode by the shaded area. As can be seen the lead-lag regressing mode is sensitive to the amount of gimbal damping only at the modal crossovers or crossings, and at low rotor speeds. The weak instability associated with the lead-lag and flap regressing mode coalescence is shown in these curves, and unstable conditions were actually encountered for two of these configurations.

The lead-lag regressing mode frequency behavior is unchanged as body roll stiffness is varied. However, the body roll mode and flap regressing mode frequencies are shifted upwards in frequency as roll stiffness is increased. The upward shift in the flap regressing mode results in changing the rotor speed at which coalescence with the lead-lag regressing mode occurs. The body roll mode shows a strong dependence on rotor speed and even for the configuration with the softest roll spring the roll and lead-lag regressing modes are well separated in frequency; consequently no mechanical instability of the ground resonance type occurs. The lead-lag regressing mode damping is relatively unchanged as body roll stiffness is increased, except for the shift in the location of the weak instability due to the flap and lead-lag mode coalescence.

The agreement between the theoretical predictions and experimental data for modal frequency is excellent. Even when the scale is expanded as in the case of the lead-lag and flap regressing mode coalescence the correlation is still very good. The lead-lag regressing mode data show the best agreement, whereas the greatest difference between theory and experiment is for the body roll mode, particularly the configuration with $\omega_{\phi 0} = 4.11$ Hz. The agreement between the theory and experiment is not as good for the lead-lag regressing mode damping. The lead-lag regressing mode data show considerable scatter and in general the theory overpredicts the level of

damping. The weak instability that occurs at the lead-lag and flap regressing mode coalescence is evident in the damping data of figures 9 to 11, but the difference in rotor speed between theory and experiment for the one unstable point in figure 10(b) is inexplicable. It is interesting to note that some of the larger differences between theory and experiment occur in regions where the predicted lead-lag regressing mode damping is most sensitive to body damping. In particular, it appears that for body frequencies of 0.75 and 1.89 Hz, a higher damping level would improve the correlation.

In a few test conditions the damping showed significant nonlinear behavior. In these cases the damping was initially large and as the amplitude of the motions decreased the damping also decreased. In this sense the damping appeared directly proportional to amplitude. For the purposes of this discussion this characteristic will be referred to as a positive nonlinearity. (The damping in the gimbal bearings, however, is inversely proportional to amplitude and is termed a negative nonlinearity; see appendix A.) These cases are shown in the figures as data points located at the initial damping level with an arrow extending to the final damping level. This notation is somewhat crude, and is included only to provide an indication of where obvious nonlinear damping behavior was observed and of its extent. Although the data for these conditions appeared nonlinear there are alternative explanations for this behavior. One possibility is that data taken in the vicinity of steep gradients of damping with rotor speed showed apparent nonlinear behavior which in fact was due to slight variations in rotor speed. An additional possibility is that both the flap and lead-lag regressing modes were excited for these conditions and their combined decay gave the appearance of nonlinear behavior.

Lead-lag progressing mode. - For one roll stiffness condition ($\omega_{\phi 0} = 1.89$ Hz), the model was excited at its lead-lag progressing frequency and estimates were made of the lead-lag progressing mode frequency and damping. These are shown in figure 13 which is the same as figure 10 except for the extended scales. The frequency shows good agreement with the theoretical predictions up to about 500 rpm, after which the theory significantly overpredicts the experimental values. The theoretical predictions, however, assume that the pitch degree of freedom is absent, and it is reasonable to expect that the lead-lag and flap progressing modes might very well be affected by the actual pitch stand frequency which is approximately 27 Hz. If the pitch degree of freedom is added to the theoretical predictions, as shown by the dashed lines in these figures, it can be seen that the frequency data and theory now agree, although the agreement is not as good as for the other modes previously discussed.

The damping estimates shown in figure 13(b) show an initial dip at about 400 rpm and then a rapid increase in damping level with rotor speed. This dip, which is due to the modal crossover with the flap progressing mode, is evidenced in the theoretical prediction; but the subsequent rapid increase in damping is not predicted. If the pitch degree of freedom is included, however, the theoretical model shows much better agreement with the experimental damping, although it appears that the damping estimate of the stand-pitch mode is probably too high.

Tantalum Blades with Pitch and Roll Freedom

The tantalum stub blade configuration was tested with the pitch and roll springs set to give approximately the same nonrotating body frequencies. The experimental estimates of frequency and damping are shown in figure 14. The general character of the frequency data is much the same as for the roll freedom alone case, except that the body pitch mode is lower in frequency than the body roll mode. The body pitch and lead-lag regressing modes coalesce at about 860 rpm and mechanical instability results. As shown in figure 14(b) the lead-lag regressing mode rapidly becomes unstable, and it was necessary to use the automatic snubbing capability of the model for these data points. Interestingly enough there is no appearance of a weak instability at the crossing of the lead-lag and flap regressing modes as in the roll alone case. The agreement of the theory with the experimental frequency measurements for this case is very good. However, the theory predicts that the body pitch and lead-lag regressing modes approach and coalesce well into the unstable region, while the experimental data indicate that this approach occurs at a lower rotor speed.

The lead-lag regressing mode damping data shown in figure 14(b) maintain a relatively uniform level until the unstable region is approached, and then the damping rapidly decreases. The scatter in the data is somewhat improved over the roll alone tests, but this improvement is exaggerated by the ordinate scale contraction. As the instability is approached, the damping in the lead-lag regressing mode is sensitive to the amount of excitation. In the unstable region some of the data points show a negative nonlinearity. The correlation between theory and experiment is very good, particularly the predicted stability boundary. Changes in the amount of gimbal damping have only a slight effect upon modal damping.

Aerodynamic Blades with Roll Freedom

The model was tested with conventional blades of aerodynamic cross-section with the pitch gimbal locked out. Only one roll spring stiffness and one blade pitch angle were tested. The frequency and damping for this configuration are shown in figure 15. The character of the modal frequencies is considerably changed from the tantalum stub blade case. The lead-lag regressing mode changes frequency more quickly with rotor speed due to the decrease in the effective hinge offset. The resonance with one-per-rev has now decreased to 440 rpm. The flap regressing mode is no longer observable with the excitation method used in this experiment, and the theory predicts that its modal frequency goes to zero and it becomes critically damped at 795 rpm. The body roll mode appears independent of rotor speed, and the coupled rotor-body system becomes unstable where this mode is proximate to the lead-lag regressing mode. The modal frequency data show good agreement with the theory with some minor differences. The theory underestimates the body roll mode frequency over most of the rotor speed range, particularly in the unstable region. However, within the unstable region, frequency estimates of the stable body mode are particularly difficult in the presence of the unstable lead-lag regressing mode; therefore, discrepancies in this region

are not surprising. The lead-lag regressing mode shows good agreement between experiment and theory. As rotor speed is increased the lead-lag regressing mode prediction underestimates the experimental data. It is suggested that this is due to flexibility in the model blades that is not accounted for in theory.

The experimental estimates of the lead-lag regressing mode damping in figure 15(b) show that the damping level remains relatively constant until the onset of the instability. The mode is then unstable over a range of about 85 rpm and then becomes stable again. The damping does not return to its previous level beyond the region of instability. The experimental data show nonlinearities in damping and sensitivity to excitation level at the boundaries of the unstable region. At the lower boundary, the damping shows a negative nonlinear character, while the damping shows positive nonlinear behavior at the upper bound. The correlation of theory and experiment is good, the theory showing the proper damping level below the unstable region and the lower stability boundary. At higher rotor speeds, the theory underestimates the amount of unstable damping, and does not correctly predict the upper stability boundary. The theory also overpredicts the recovery in damping level. A possible reason for this discrepancy is that the theoretical model assumes a symmetrical airfoil at zero pitch angle, while the model employed a cambered airfoil with $c_q \approx 0.15$ at zero pitch angle. The resulting differences in inflow may explain some of this difference. Although the lead-lag regressing mode damping is sensitive to the amount of body damping in the unstable region and beyond, it does not appear that this provides a suitable explanation of the differences between theory and experiment.

Aerodynamic Blades with Pitch and Roll Freedom

Low thrust, $\theta = 0^\circ$. - The model was tested with both pitch and roll freedom using the aerodynamic blades. The spring stiffnesses used for the pitch and roll degrees of freedom were identical to the configuration tested with the tantalum stub blades; however, because the rotor mass was reduced with the aerodynamic blades the body frequencies increased correspondingly. The experimental frequency and damping estimates for this configuration are shown in figure 16. The character of the modal frequencies is little changed from the aerodynamic blade configuration with roll freedom alone, except for the addition of the pitch mode. This mode is somewhat lower in frequency than the body roll mode, and shows the same invariance with rotor speed. The region of aeromechanical instability is extended to lower rotor speeds due to the coupling of the body pitch mode with the lead-lag regressing mode. The unstable region extends to higher rotor speeds as well. The agreement between experiment and theory is quite good, with a slight underprediction of the frequency of both body modes. The prediction of the body mode frequencies is not as satisfactory at low rotor speeds. As in the roll alone configuration, the theoretical model underpredicts the experimental value of the lead-lag regressing mode frequency at high rotor speeds. As discussed previously the experimental estimates of body mode frequencies in the unstable region are unreliable.

The damping of the lead-lag regressing mode is quite similar to the case of roll alone. The damping maintains a relatively even level until the region of instability is reached and then shows an incomplete recovery to its former level beyond the unstable region. As in the roll-alone case, some of the damping values show a negative nonlinear character for the lower rotor speeds in the unstable region, while positive nonlinearities are seen at higher rotor speeds. The correlation of the experimental values and the theory is good particularly at lower rotor speeds and in the prediction of the lower stability boundary. As in the roll-alone case the theory underpredicts the unstable damping within the region of the instability.

High thrust, $\theta = 8.9^\circ$. - The model was tested for one condition with the rotor producing substantial thrust, although over a reduced range of rotor speed. Experimental estimates of the frequency and damping are shown in figure 17. The modal frequencies show much the same character as for the low-thrust case with a slight increase in the body roll mode frequency being the only significant difference. The correlation of experiment and theory is good.

The lead-lag regressing mode damping is shown in figure 17(b). These data show major changes over the low-thrust case. Below the unstable region, the mode shows a significant increase in damping level instead of keeping a constant level as in the low-thrust case. The change in damping at the lower stability bound is very rapid and substantial unstable damping values are obtained in the unstable region. As rotor speed is increased, the damping increases at a faster rate than in the low-thrust condition. As in the other aerodynamic blade configurations, negative nonlinear damping occurs near the lower stability boundary, and positive nonlinear damping occurs near the upper boundary. The correlation is quite good, the theory showing all the major features of the data. The lower stability boundary and both the positive and negative extent of the damping are well represented. The theory, however, underestimates the amount of damping that was measured at the higher rotor speeds, a trend that is opposite to what was seen in the low-thrust case. Compared to the low-thrust case the effect of pitch angle is to increase both the size of the unstable region and the amount of unstable damping. This agrees with the general trends identified in reference 2.

CONCLUSIONS

The following conclusions are offered:

1. Modal frequency data of excellent quality were obtained for the rotor lead-lag regressing mode, and the body pitch and roll modes. In the case of simulated vacuum tests good modal frequency data were obtained for the rotor flap regressing mode as well.

2. Damping data of good quality were obtained for the lead-lag regressing mode, with the exception of some test rotor speeds where the modal damping showed sensitivity to excitation level or nonlinearity.

in damping with amplitude. Body mode damping data were poor and reflected the nonlinear behavior of the gimbal ball bearings.

3. In the case of simulated vacuum testing with roll freedom alone, the data show a weak instability where the lead-lag and flap regressing modes are proximate. This instability was predicted in reference 2 for rotors in a vacuum.

4. Mechanical instability of the classical ground resonance type was obtained during simulated vacuum testing with pitch and roll freedom.

5. Aeromechanical instabilities were encountered during tests with conventional airfoil blades both at low and normal thrust levels. Thrust tends to destabilize the rotor-body system as shown in reference 2.

6. All data were correlated with the theoretical model of reference 9 and in general good correlation was obtained. The quality of the correlation was better for simulated vacuum testing than with aerodynamics included. This implies that the accuracy of the data was degraded with aerodynamics included, or that the theoretical modeling of blade aerodynamics is not as accurate as the modeling of the structural and inertia terms.

7. The use of tantalum blades with a circular cross section proved to be an effective means of simulating rotor testing in a vacuum. The effective Lock number of these blades was reduced to 0.2% of the blades with a conventional airfoil.

8. The transformation of individual blade bending moment signals to multi-blade coordinates in the fixed system provided a means of directly observing the rotor progressing and regressing modes. This capability contributed to the success of the experiment.

9. The use of a snubbing mechanism to lock out body motions when encountering coupled rotor-body instabilities provided a safe means of testing well into the unstable regimes. The inclusion of automatic snubbing based on blade lead-lag bending moment was essential to the completion of the experiment.

10. The ball bearings used in the gimbal frame to provide pitch and roll freedom exhibited nonlinear damping of the Coulomb or dry friction type. Flexural pivots to replace these bearings, or a reduction in bearing size or number of balls is required to eliminate the influence of this nonlinear damping.

APPENDIX A
EXPERIMENTAL MODEL PROPERTIES

ROTOR PROPERTIES

Geometric and Miscellaneous Properties

The rotor geometric properties are tabulated in table 2 for both the aerodynamic blade and tantalum stub blade configurations.

TABLE 2. - ROTOR GEOMETRIC PROPERTIES

Quantity	Aerodynamic blade	Tantalum blade
Rotor radius, R , cm	81.13	38.01
Blade chord, c , cm	4.19	1.26
Solidity, σ	0.0493	0.0318
Hinge offset, e/R	0.105	0.224
Root cutout, x_{co}/R	0.186	--

The hinge offset is defined by the center of the blade root flexures. The root cutout is the distance to the inboard edge of the blade airfoil. Miscellaneous descriptive properties of the rotor are presented in table 3.

TABLE 3. - ROTOR DESCRIPTIVE PROPERTIES

Quantity	Aerodynamic blade	Tantalum blade
Blade number, b	3	3
Airfoil section	NACA 23012	Circular
Lift curve slope, a	5.73	0.0
Profile drag coefficient	0.0079	1.0
Lock number	7.95	0.0182

The profile drag coefficient for the aerodynamic blade was estimated from steady blade deflection data (ref. 10). The Lock number includes the effect of the profile drag coefficient as discussed in the body of the report. The blade is untwisted. The height of the rotor plane above the gimbal axes is $h = 24.1$ cm.

Mass Properties

The blade mass and inertia properties are given in table 4; included are both the blade and the root flexure hardware outboard of the flap flexure centerline.

TABLE 4. - BLADE MASS AND INERTIA PROPERTIES

Quantity	Aerodynamic blade	Tantalum blade
Mass, m_b , g	332.	699.
Centroid of mass with respect to centerline, x_{cn}/R	0.315	0.573
Flapping and lead-lag inertia, I , $g\text{-m}^2$	16.1	17.7
Pitch inertia, I_a , $g\text{-m}^2$	0.00224	0.00285
Rotor polar inertia, J_r , $g\text{-m}^2$	76.5	12.0

Blade mass was measured by weighing the blade and root flexure hardware. The centroid, flapping and lead-lag inertias, and pitch inertia for the aerodynamic blade were calculated from mass and dimensional data for the blade root hardware, and by measurements reported for the blade alone in reference 14. The blade flapping and lead-lag inertias were the same to within the accuracy of the measurements. The centroid of the tantalum blade was measured by balancing the blade on a knife edge, while the inertia was estimated from pendulum tests. The stub blade pitch inertia was calculated from its dimensional properties. The rotor polar inertia given in table 4 is for three blades together. It was calculated including the hub and root hardware inboard of the flapping axis (these constitute only 4% and 3% of the total polar inertia for the aerodynamic and tantalum blades respectively), but excluding the effects of the drive shaft, bellows couplings, and transmission gear train. This assumption was checked by measuring both pitch and roll body frequencies over a range of rotor speeds with the blade and root hardware removed; no frequency change due to gyroscopic coupling could be determined.

Stiffness Properties

The flap and chordwise stiffness of the blade root flexure and blade are shown in table 5. The flapping root flexure length is 1.212 cm, and the

TABLE 5. - FLAP AND CHORDWISE STIFFNESS (EI), N-cm²

Quantity	Flap	Chord
Root flexure	8.35×10^2	1.55×10^3
Aerodynamic blade	6.54×10^4	1.77×10^6
Tantalum blade	2.34×10^6	2.34×10^6

lead-lag root flexure is 0.699 cm in length. The tabulated aerodynamic blade stiffness properties extend from B.S. 20.17 cm to the tip, while for the tantalum blade the properties run from B.S. 13.77 to the tip.

Frequency and Damping

The frequency and damping of the rotor blades were measured under non-rotating conditions. The blade frequencies are presented in table 6. The first torsion mode and higher flap and lead-lag modes were obtained from

TABLE 6. - NONROTATING BLADE FREQUENCIES, Hz

Blade	Mode	Flap	Lead-lag	Torsion
Aerodynamic	1	3.10	6.58	342.
	2	32.	150.	--
	3	96.	357.	--
Tantalum	1	3.01	6.39	--

shake tests of a single blade and root flexure. The mean value of the first flap and lead-lag mode frequencies were measured with the blades installed on the model, with the exception of the tantalum blade flap mode which could not be obtained due to droop-stop restraint. This frequency was calculated as:

$$(\omega_{\beta 0})_{\text{tant}} = (\omega_{\beta 0})_{\text{aero}} \frac{(\omega_{\zeta 0})_{\text{tant}}}{(\omega_{\zeta 0})_{\text{aero}}}$$

The mean damping of the blades was (in percent critical damping):

$$(\eta_{\zeta})_{\text{aero}} = 0.362 \%$$

$$(\eta_{\zeta})_{\text{tant}} = 0.185 \%$$

BODY PROPERTIES

Mass and Inertial Properties

The mass of the body was measured by weighing the model without the gimbal frame or hub components. Portions of the blade root flexure inboard of the flapping flexure were weighed separately and included in the body weight. The resulting estimate is: $m_b = 19,270$ g.

The body inertias were estimated for one combination of pitch and roll spring settings. The blades and root hardware were removed, and the body mode natural frequencies determined. The spring rates were computed by measuring the model deflection under an applied moment. The inertias were then calculated assuming the body behaved as a single degree-of-freedom system, and adding the contribution of the blade root hardware inboard of the flapping hinge. The estimates of the inertias are: $I_{\theta} = 511$ g-m²; and $I_{\phi} = 187$ g-m².

The center of gravity of the body was not measured, but was assumed to be coincident with the intersection of the pitch and roll axes.

Frequency and Damping

For each test configuration, body mode frequency and damping were measured under nonrotating conditions. These frequencies, previously shown in table 1, are not uncoupled body frequencies, but rather are coupled or partially coupled frequencies. In the case of the tantalum stub blades, flapping is restrained by the blade droop stops, but lead-lag motion is unrestrained. For the aerodynamic blades, both flap and lead-lag motion couple with the body motion.

The damping of the body is strongly affected by the nonlinear damping character of the pitch and roll ball bearings. The effects of bearing damping were investigated by completely stripping the model of extraneous cables, wires, or tubes that might restrain the body, and by observing the decay of body oscillations after deflecting the model. The bearings were

free of grease or oil for these tests. A local damping coefficient was defined based on the decay per half cycle as:

$$\zeta_{\text{local}} = 200 \ln (\theta_{i+1}/\theta_i)$$

in percent of critical damping, where θ_i represents the magnitude of the first peak, and θ_{i+1} is the magnitude of the peak a half cycle later. The measured values of the local damping coefficient for pitch and roll are shown in figure 18. If the damping were linear the local damping coefficient would be invariant with amplitude. The dependency of the damping on amplitude suggests that the nonlinearity is due to Coulomb friction. If it is assumed that the source of the Coulomb friction in the bearings is due to the balls rubbing against the bearing cage then the damping term should be:

$$D = 2r_B n_B f_B$$

where r_B is the radius to the bearing race where the damping force is applied, n_B is the number of balls in the bearing, and f_B is the friction force. The first two values are known parameters of the bearing configuration; however, the friction force f_B depends on cage restraining force and the friction coefficient between the balls and cage and is unknown. As the damping term is dependent on only the sign of velocity, the differential equation describing a single-degree-of-freedom system is nonlinear. There is, however, a closed form solution (ref. 15) which may easily be expressed in terms of a local damping coefficient.

$$\zeta_{\text{local}} = 200 \ln \left(\frac{\theta_i - \frac{4r_B n_B f_B}{K}}{\theta_i} \right)$$

where K is the body stiffness. If a value for the friction force f_B is arbitrarily selected to fit the pitch bearing data, it can be seen in figure 18 that the hypothesis offered here provides an excellent representation of the measured bearing damping. However, the predicted damping for the roll bearing is considerably in error. An examination of the roll bearing design shows that the cage only restrains alternate balls, the ones in between being free to rotate three or four diameters before encountering the cage. If it is assumed that only the 23 restrained balls in the bearing affect the damping then the agreement with the measurements is much improved. To reduce the effect of this nonlinearity it is necessary to reduce the bearing radius, the number of balls, or both. Clearly, having a lot of balls is not advantageous in this case.

Estimates of a representative body damping were difficult to obtain from the data because of the nonlinear bearing damping. Subjective estimates were made for the tantalum stub blade configurations; these values are shown in figure 19. It appears that the effective body damping increases as body stiffness is reduced. This result is consistent with the expression for Coulomb friction damping given above which shows that the local damping coefficient increases as stiffness is reduced.

APPENDIX B

INPUT DATA FOR CORRELATION MODEL

The input data used in the theoretical model of reference 9 are described in table 7. Most of the values in table 7 were calculated directly

TABLE 7. - CORRELATION MODEL INPUT DATA

Parameter	Aerodynamic blade	Tantalum blade
L, cm	72.01	28.88
I, g-m ²	15.63	16.60
Ω_0 , sec ⁻¹	104.7	104.7
$EI_f/I\Omega_0^2\ell$.03592	.03481
$EI_c/I\Omega_0^2\ell$.1594	.1567
$GJ/I\Omega_0^2\ell$.6038	.5682
$EA\ell/I\Omega_0^2$	395.2	371.9
ℓ/L	.01683	.04195
e/ℓ	6.525	6.525
$m_b L^2/I$	7.688	3.509
I_α/I	.001434	.001718
x_b	.2282	.4382
x_c		
$g/\Omega_0^2 L$.007241	.003094
$\rho c L^4(a+c_{d0})/I$	5.061	.006496
σ	.04933	.03179
c_{d0}	.0079	1.0
a	5.73	.0
$m_B L^2/I$	639.1	96.8
I_ϕ/I	11.93	11.23
I_θ/I	32.65	30.73
h/L	.3351	.8355
$k_z L^2/I\Omega_0^2$	1.	1.
ℓ_x/L	(a)	(a)
ℓ_y/L	(a)	(a)
η_z	.0035	.00185
$\eta_{\phi x}$.03	.03
$\eta_{\phi y}$.03	.03

^aSelected to match body frequency.

from the model data of appendix A. The blade nondimensional flap and lead-lag stiffness were computed from the nonrotating, uncoupled blade frequency data rather than from the structural properties of the root flexures. The nondimensional vertical spring spacings were selected to match the measured body frequencies. For the tantalum blade configurations the spacings were computed assuming that the blade was drooped 2° and restrained from moving. The same spacings were used for aerodynamic blade configurations, as the actual spring settings were kept the same between the two configurations. Body pitch and roll damping were set to 3% critical, rather than trying to match the nonlinear values.

REFERENCES

1. Coleman, Robert P.; and Feingold, Arnold M.: Theory of Self-Excited Mechanical Oscillations of Helicopter Rotors with Hinged Blades. NACA TR-1351, 1958.
2. Ormiston, Robert A.: Aeromechanical Stability of Soft Inplane Hingeless Rotor Helicopters. Paper 25, Third European Rotorcraft and Powered Lift Aircraft Forum; Aix-en-Provence, France, September 1977.
3. Lytwyn, R. T.; Miao, W.; and Wolitch, W.: Airborne and Ground Resonance of Hingeless Rotors. J. American Helicopter Soc., Vol. 16, No. 2, April 1971.
4. Donham, R. E.; Cardinale, S. V.; and Sachs, I. B.: Ground and Air Resonance Characteristics of a Soft Inplane Rigid Rotor System. J. American Helicopter Soc., Vol. 14, No. 4, October 1969.
5. Baldock, J. C. A.: Some Calculations for Air Resonance of a Helicopter with Non-articulated Rotor Blades. RAE Technical Report 72083, August 1972.
6. Burkhams, John E.; and Miao, Wen-Liu: Exploration of Aeroelastic Stability Boundaries with a Soft-in-Plane Hingeless-Rotor Model. J. American Helicopter Soc., Vol. 17, No. 4, October 1972.
7. Miao, Wen-Liu; and Huber, Helmut B.: Rotor Aeroelasticity Coupled with Helicopter Body Motion. NASA SP-352, February 1974.
8. Ormiston, Robert A.: Helicopter Modelling. The Aeronautical Journal, Vol. 77, No. 1. 755, November 1973.
9. Hodges, Dewey H.: A Theoretical Technique for Analyzing Aeroelastic Stability of Bearingless Rotors. Proceedings of the 19th AIAA/ASME Structures, Structural Dynamics and Materials Conference, Bethesda, Md., April 1976, pp. 282-294.
10. Bousman, W. G.; Sharpe, D. L.; and Ormiston, R. A.: An Experimental Study of Techniques for Increasing the Lead-lag Damping of Soft Inplane Hingless Rotors. Preprint No. 1035, 32nd Annual National V/STOL Forum of the American Helicopter Society, May 1976.
11. Ormiston, Robert A.; and Hodges, Dewey H.: Linear Flap-lag Dynamics of Hingeless Helicopter Rotor Blades in Hover. J. American Helicopter Soc., Vol. 17, No. 2, April 1972.
12. Hohenemser, Kurt H.; and Yin, Sheng-kuang: Some Applications of the Method of Multiblade Coordinates. J. American Helicopter Soc., Vol. 17, No. 3, July 1972.

13. Bousman, William G.: An Analog Technique for the Measurement of Damping From Transient Decay Signals. NASA TM X-73,121, June 1976.
14. Analytical and Model Investigation of Hingeless Rotor Air Stability, Vol. 1. Boeing Company, Vertol Division, December 1973.
15. Meirovitch, Leonard: Elements of Vibration Analysis. McGraw-Hill, Inc., New York, 1975.

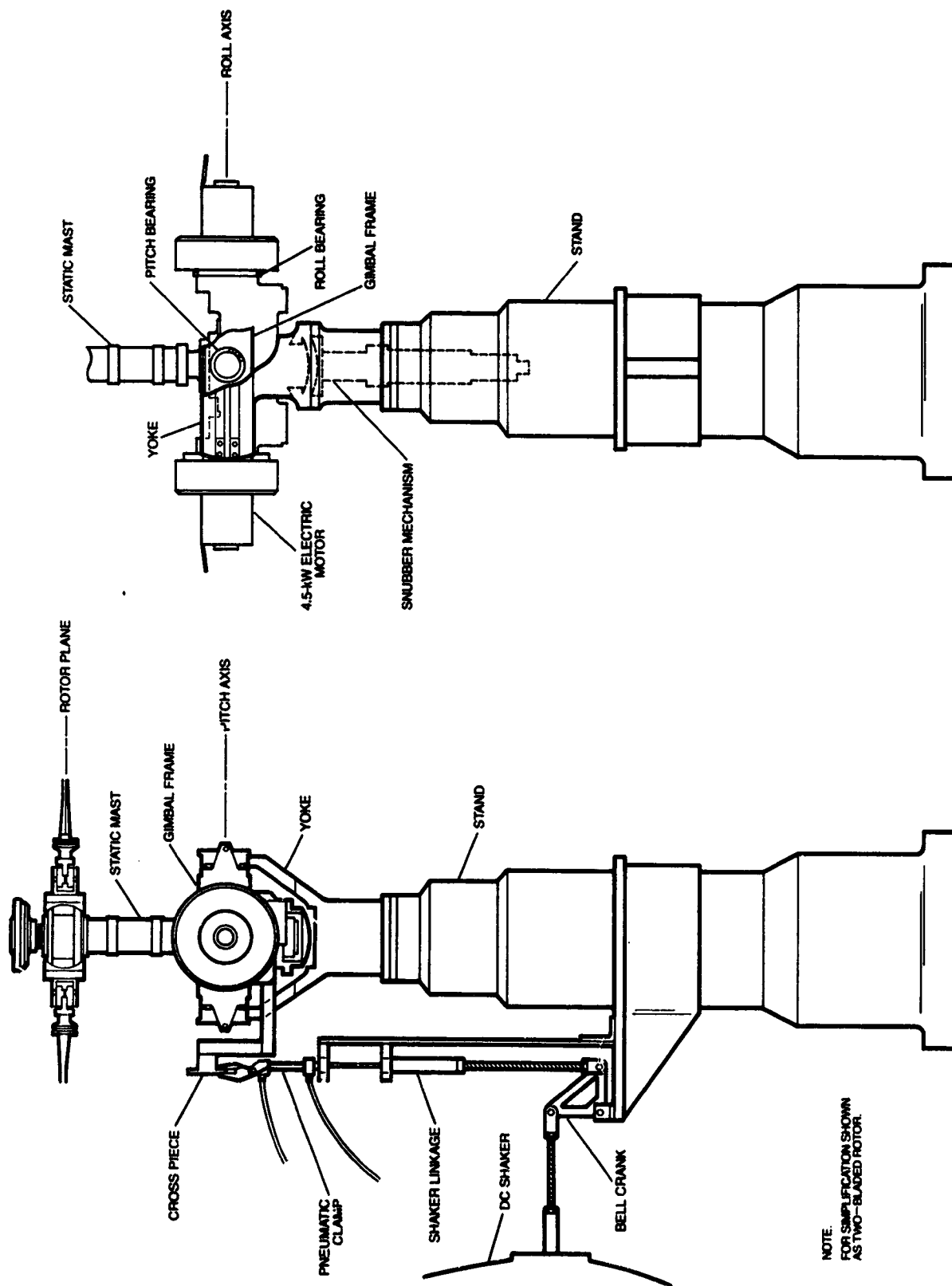


Figure 1.- Schematic two-view drawing of rotor model and test stand.



Figure 2.- 1.62-m diameter rotor model in hover test area.



Figure 4.- Close-up of blade root flexures.

ORIGINAL PAGE IS
OF POOR QUALITY

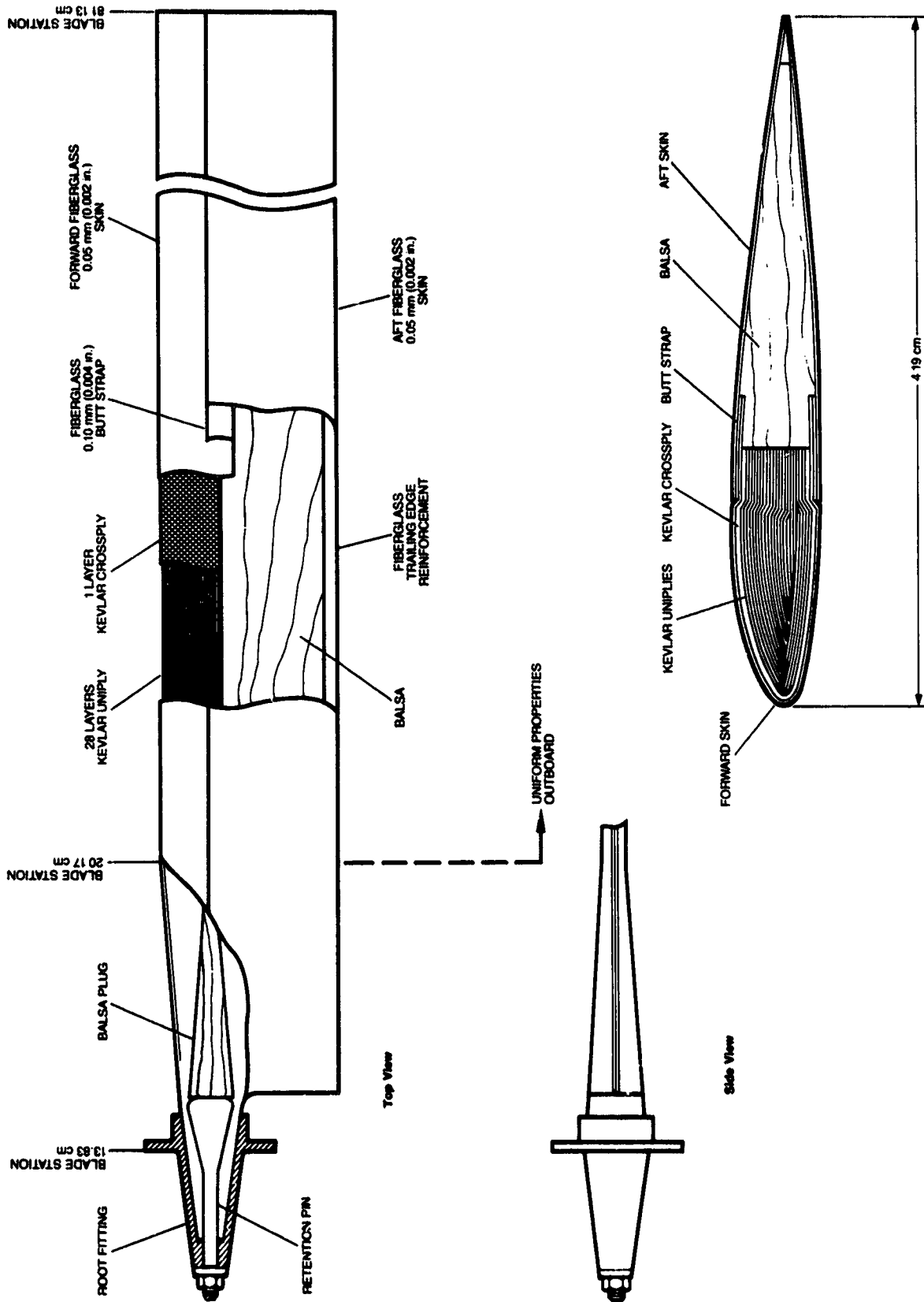


Figure 5.- Model blade construction.

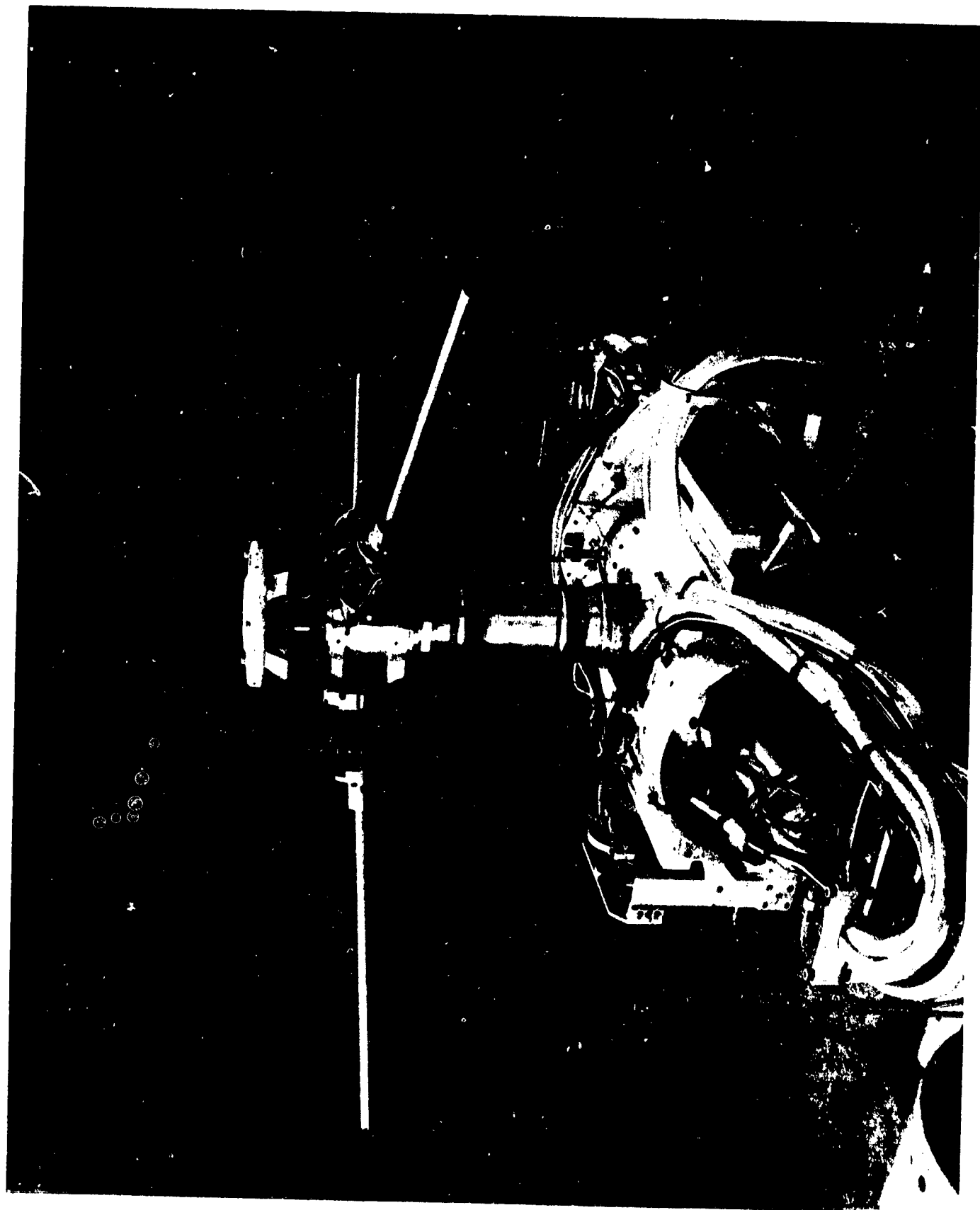


Figure 6.- Rotor model with tantalum stub blades installed.

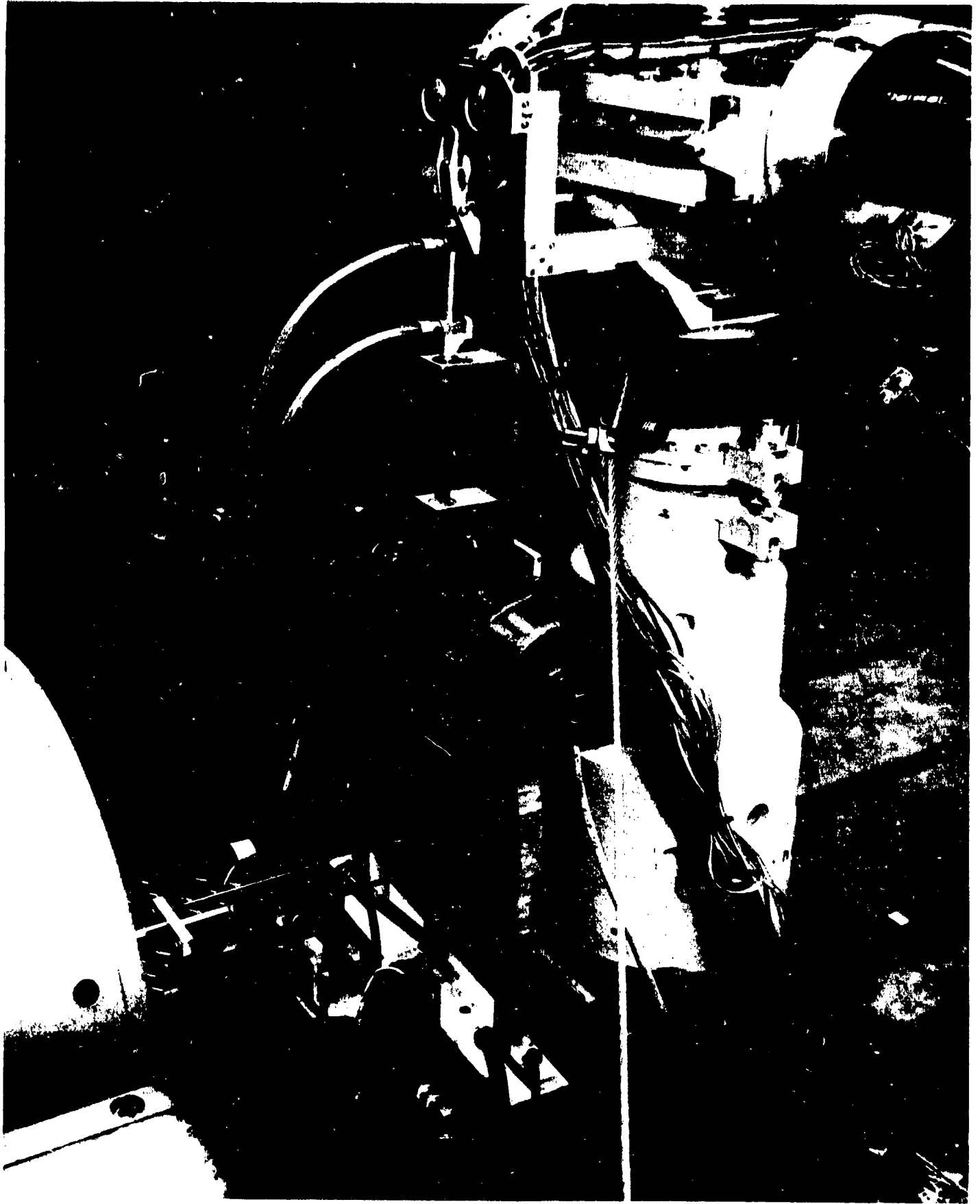


Figure 7.- Rotor model excitation set-up.

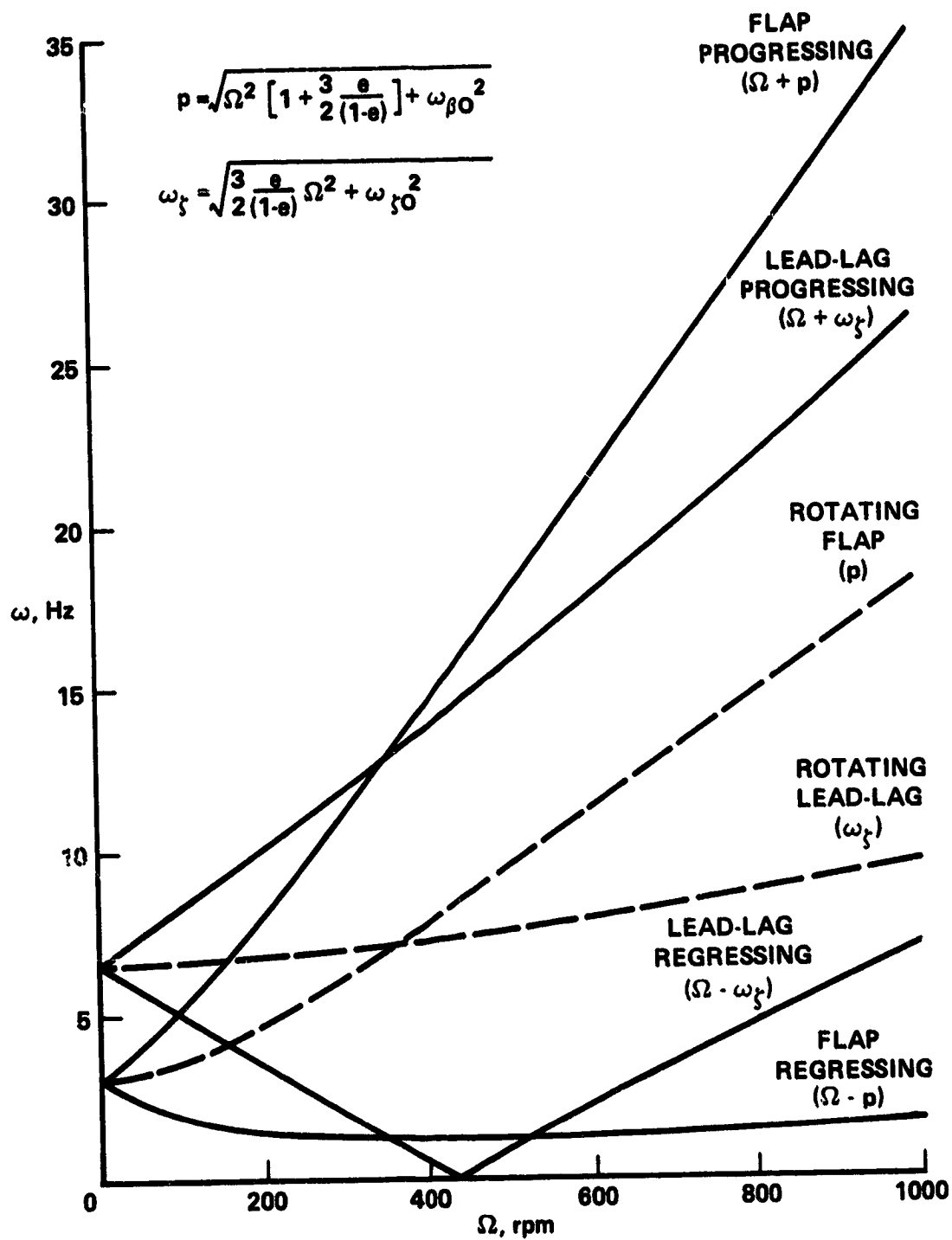
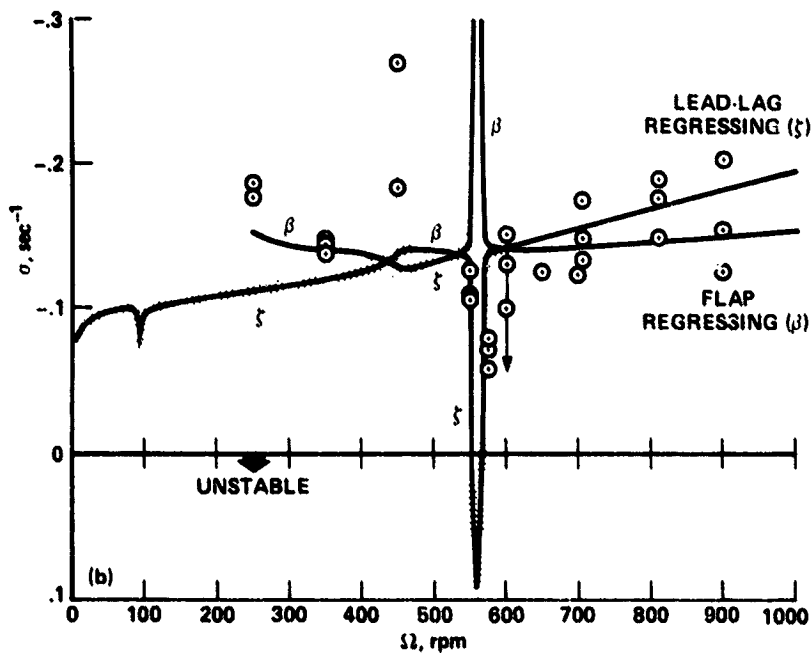
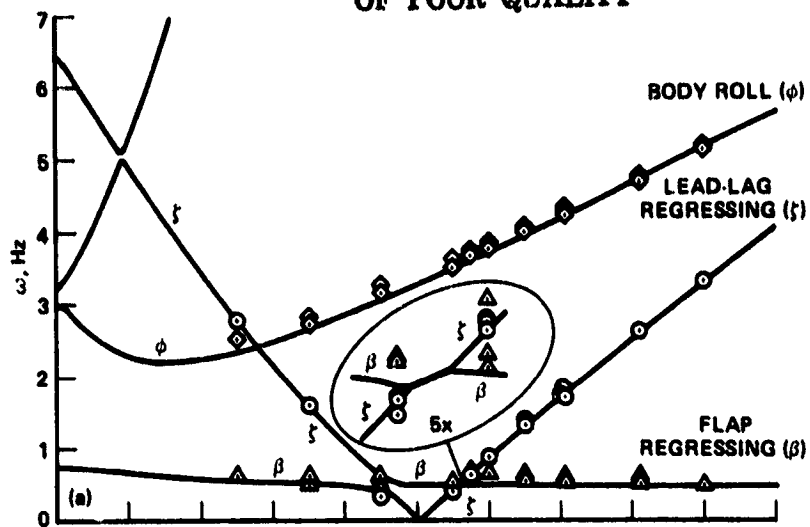


Figure 8.- Uncoupled rotor progressing and regressing mode frequencies in fixed system (rotating blade frequencies shown for clarity).

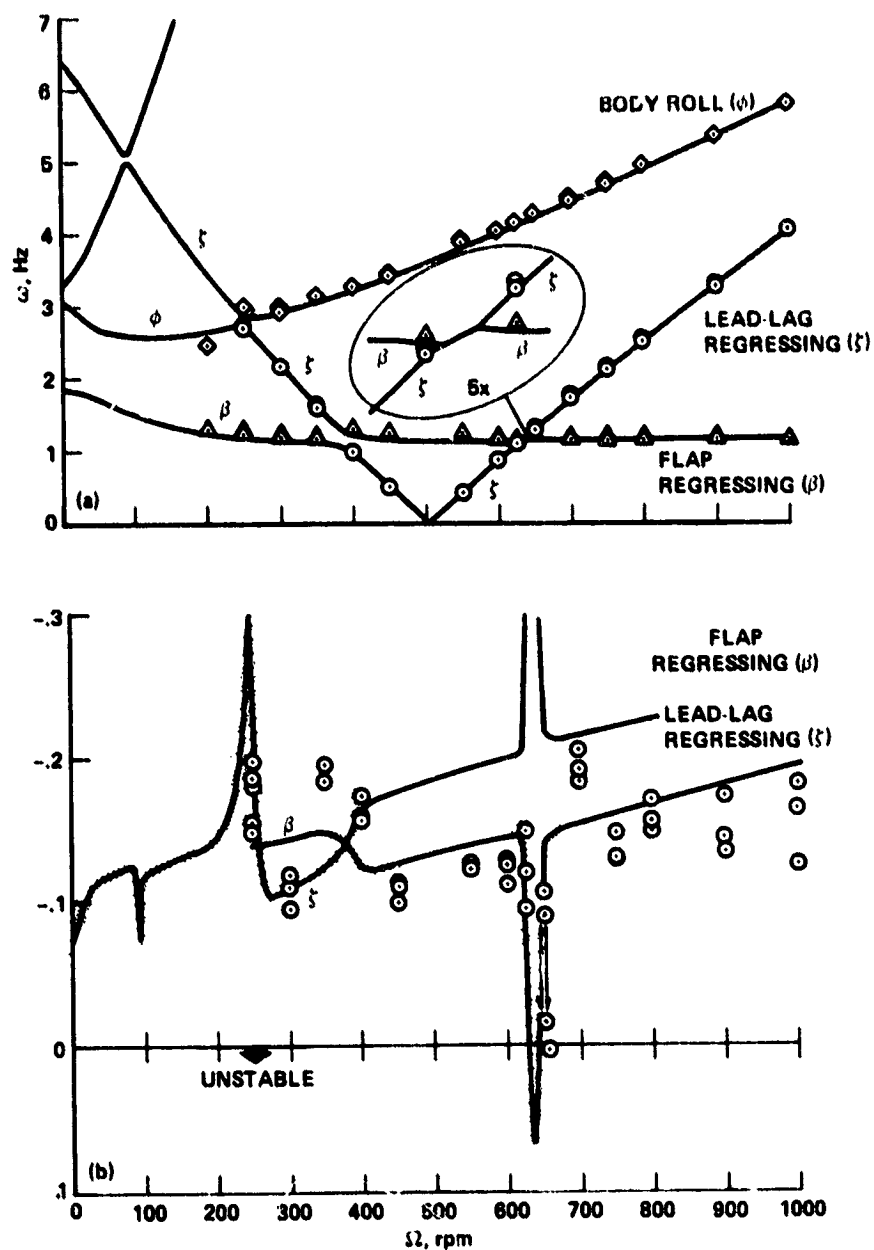
ORIGINAL PAGE 13
OF POOR QUALITY



(a) Modal frequency.

(b) Lead-lag regressing mode damping (shaded area shows effect of doubling and halving nominal body damping).

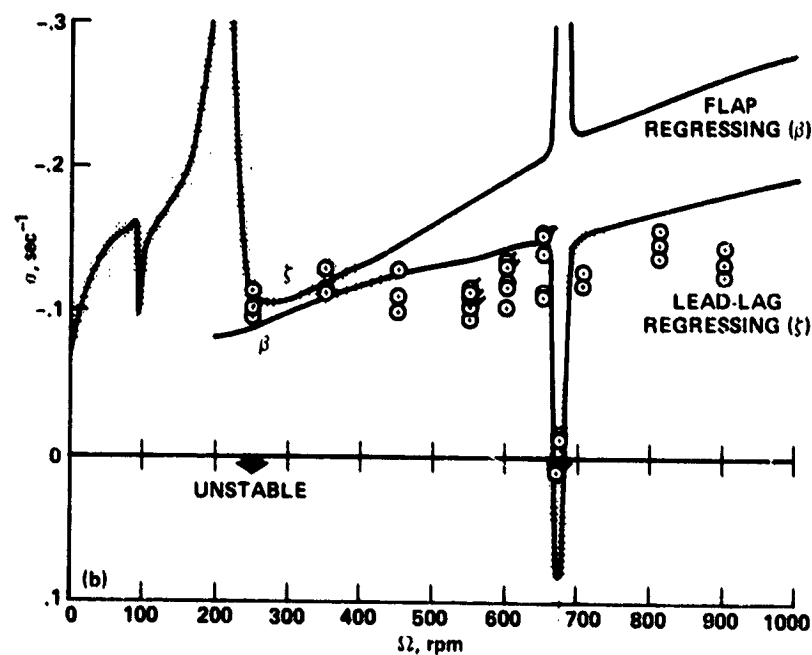
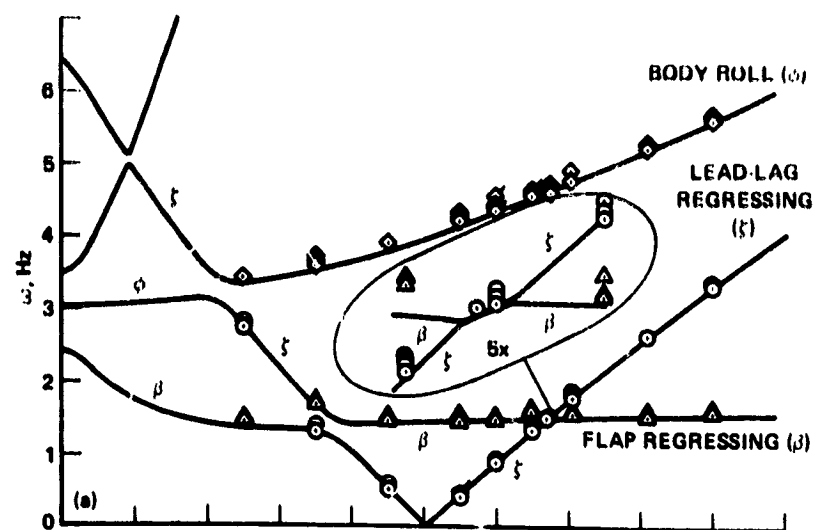
Figure 9.- Tantalum stub blades with roll freedom; $\omega_{\phi 0} = 0.75$ Hz.



(a) Modal frequency.

(b) Lead-lag regressing mode damping (shaded area shows effect of doubling and halving nominal body damping).

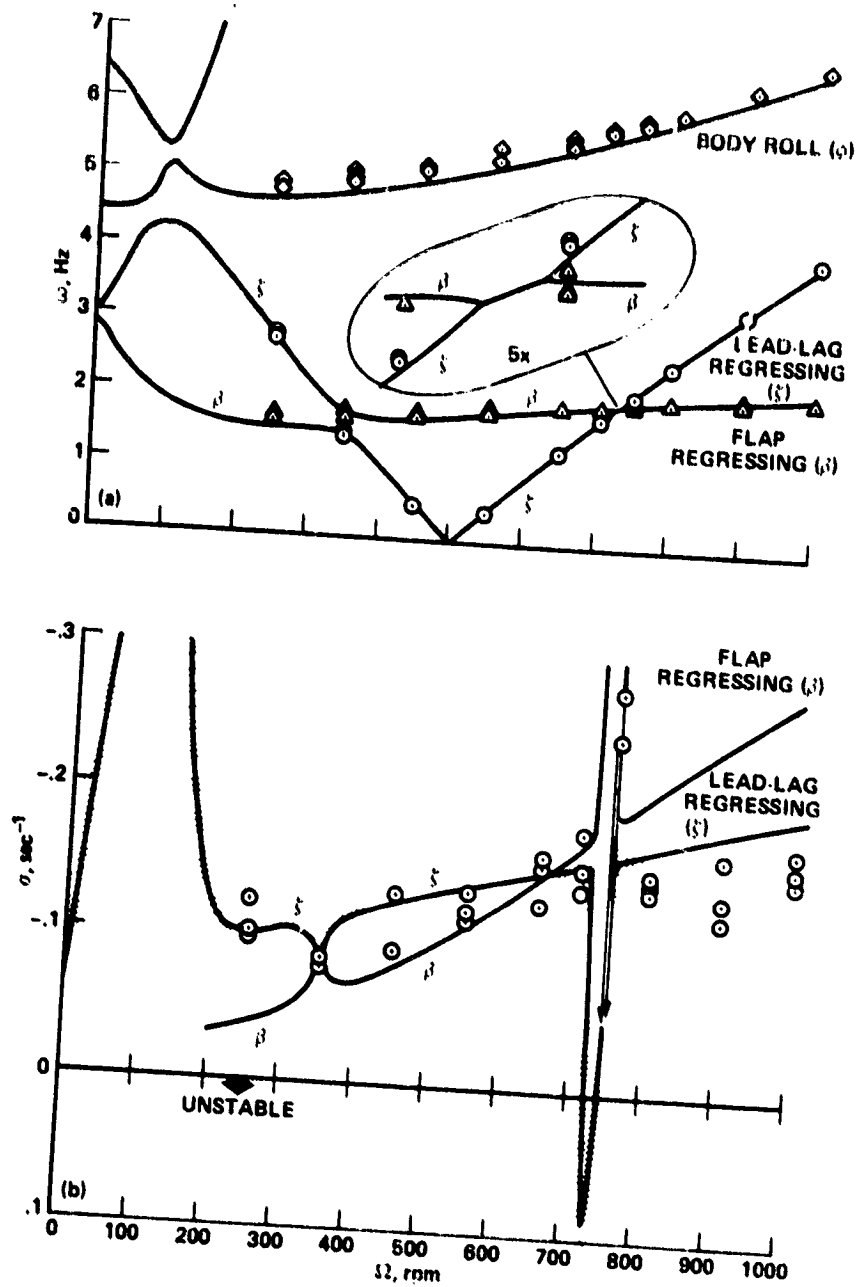
Figure 10.- Tantalum stub blades with roll freedom; $\omega_{\phi 0} = 1.89$ Hz.



(a) Modal frequency.

(b) Lead-lag regressing mode damping (shaded area shows effect of doubling and halving nominal body damping).

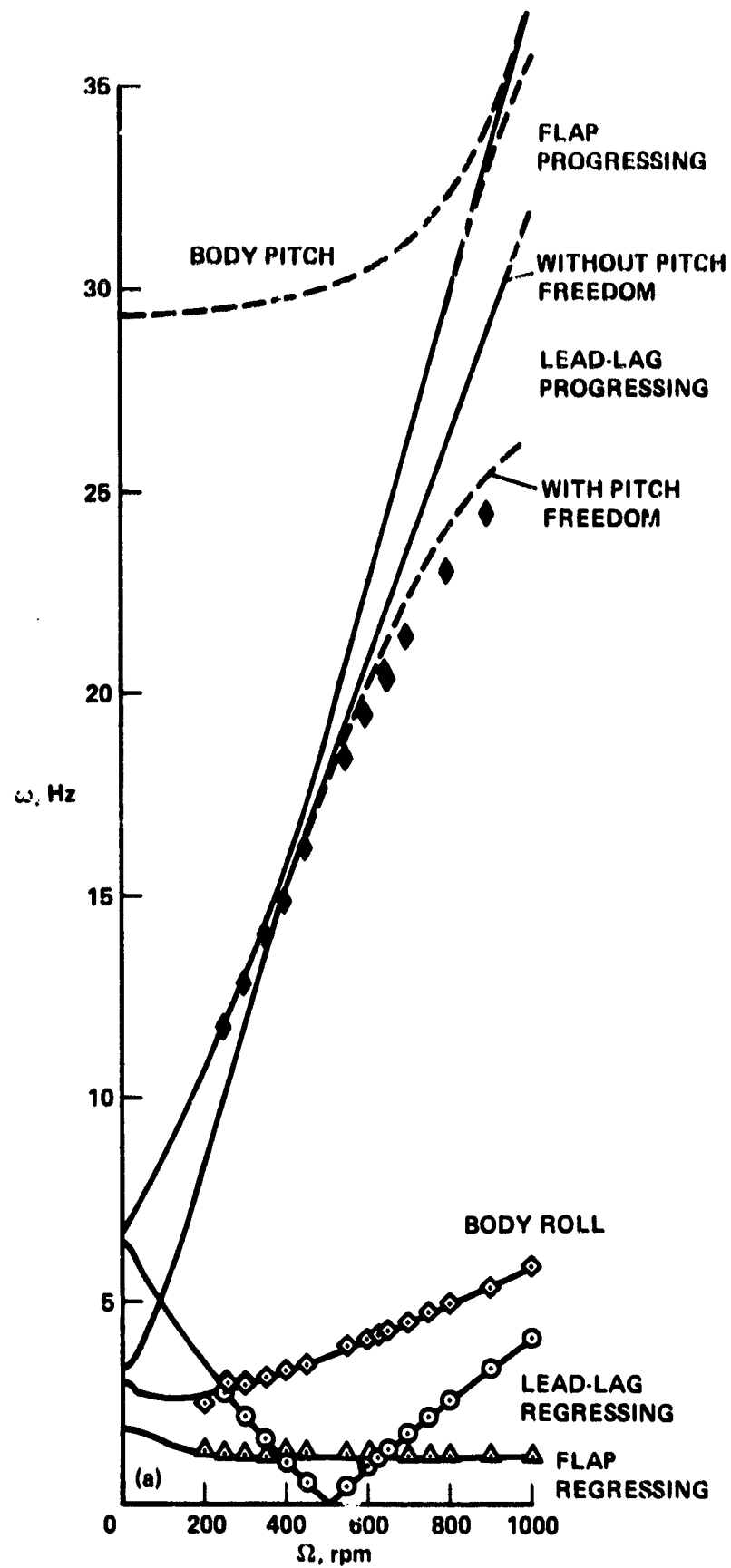
Figure 11.- Tantalum stub blades with roll freedom; $\omega_{\phi 0} = 2.60$ Hz (flagged symbols $\omega_{\phi 0} = 2.56$ Hz).



(a) Modal frequency.

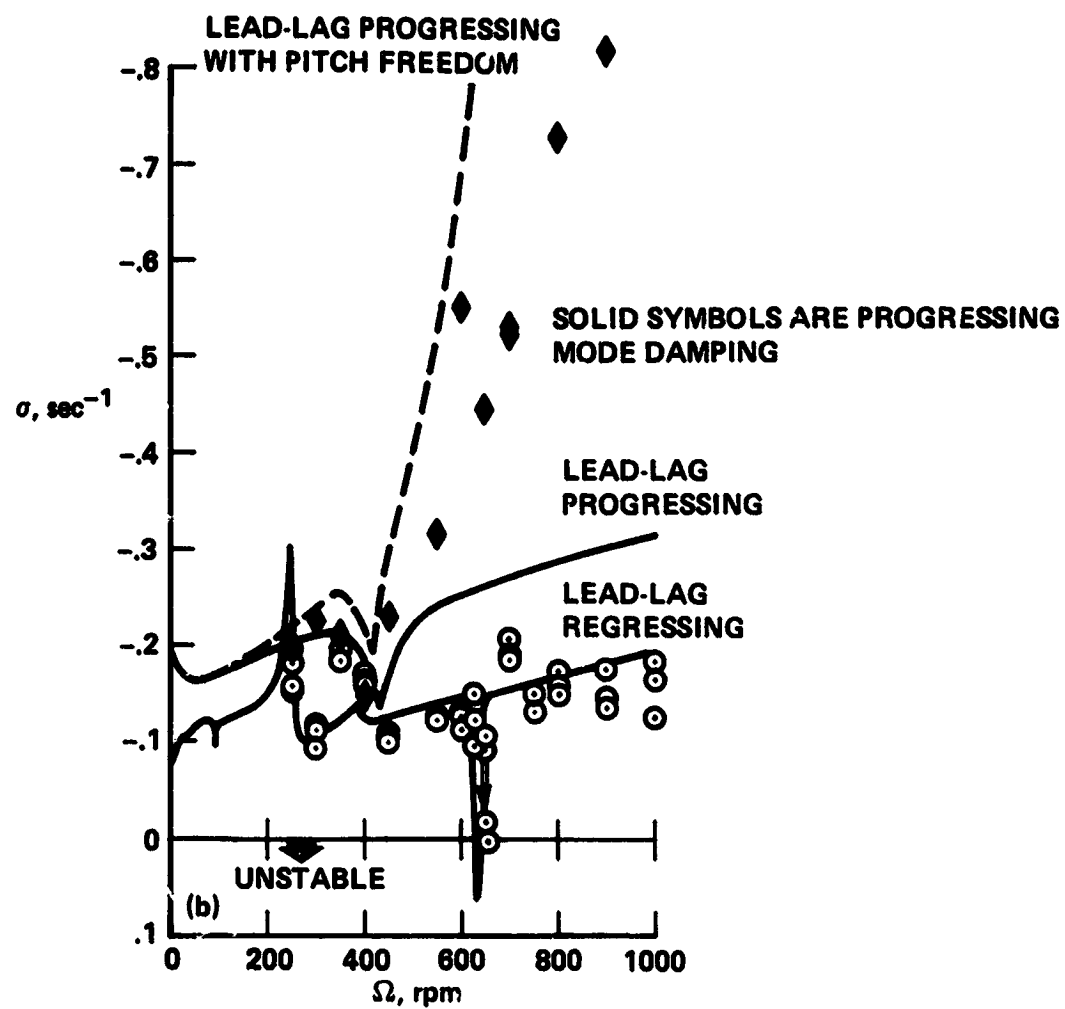
(b) Lead-lag regressing mode damping (shaded area shows effect of doubling and halving nominal body damping).

Figure 12.- Tantalum stub blades with roll freedom; $\omega_{\phi 0} = 4.11$ Hz.



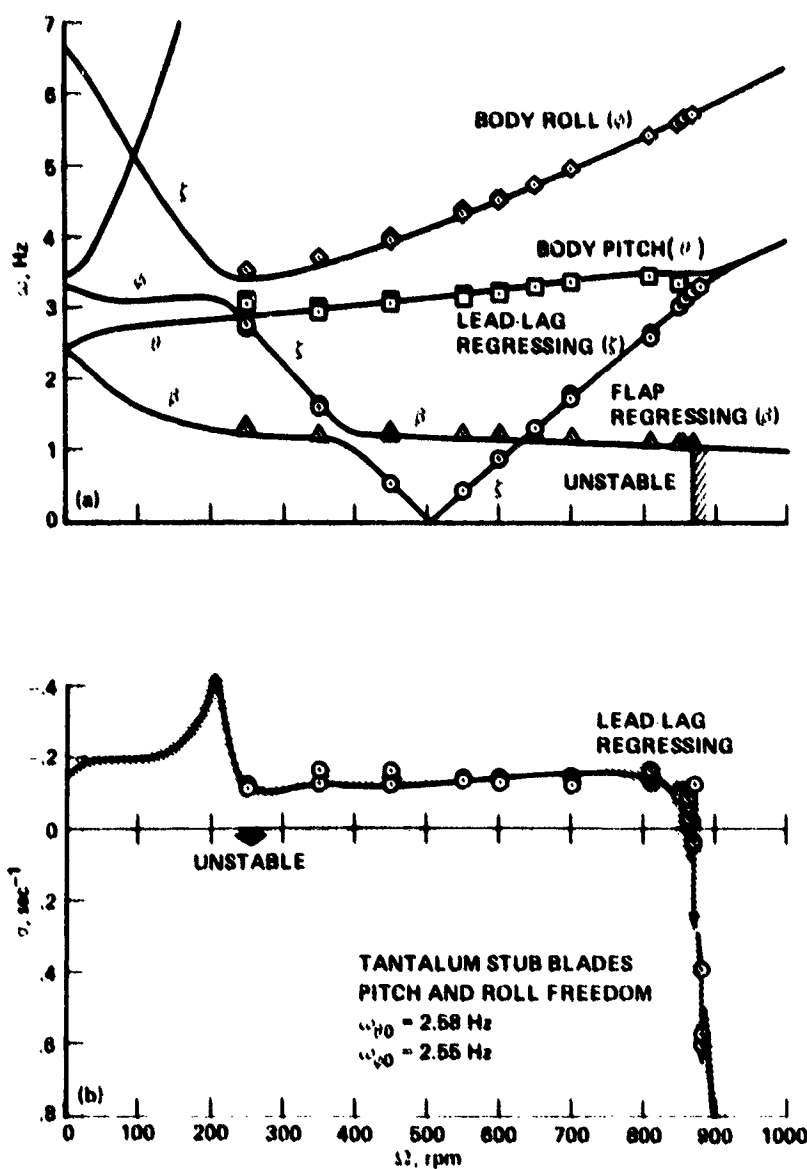
(a) Modal frequency.

Figure 13.- Tantalum stub blades with roll freedom, including progressing modes $\omega_{\phi 0} = 1.89$ Hz.



(b) Lead-lag mode damping.

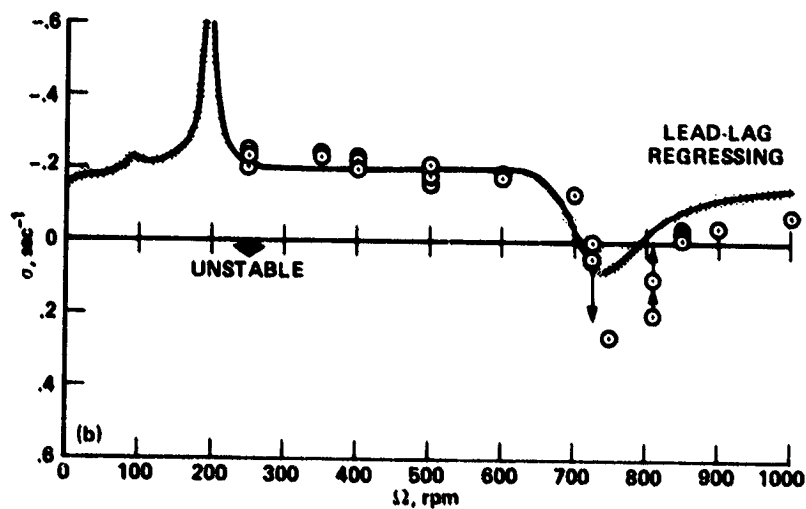
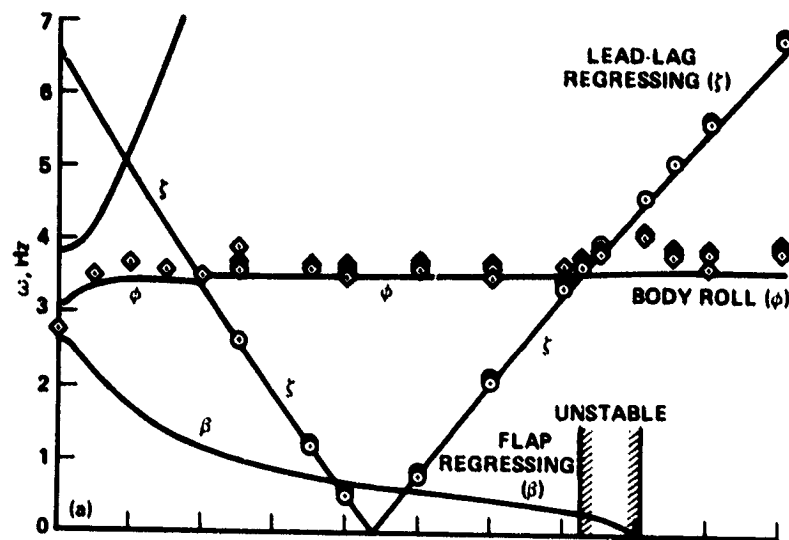
Figure 13.- Concluded.



(a) Modal frequency.

(b) Lead-lag regressing mode damping (shaded area shows effect of doubling and halving nominal body damping).

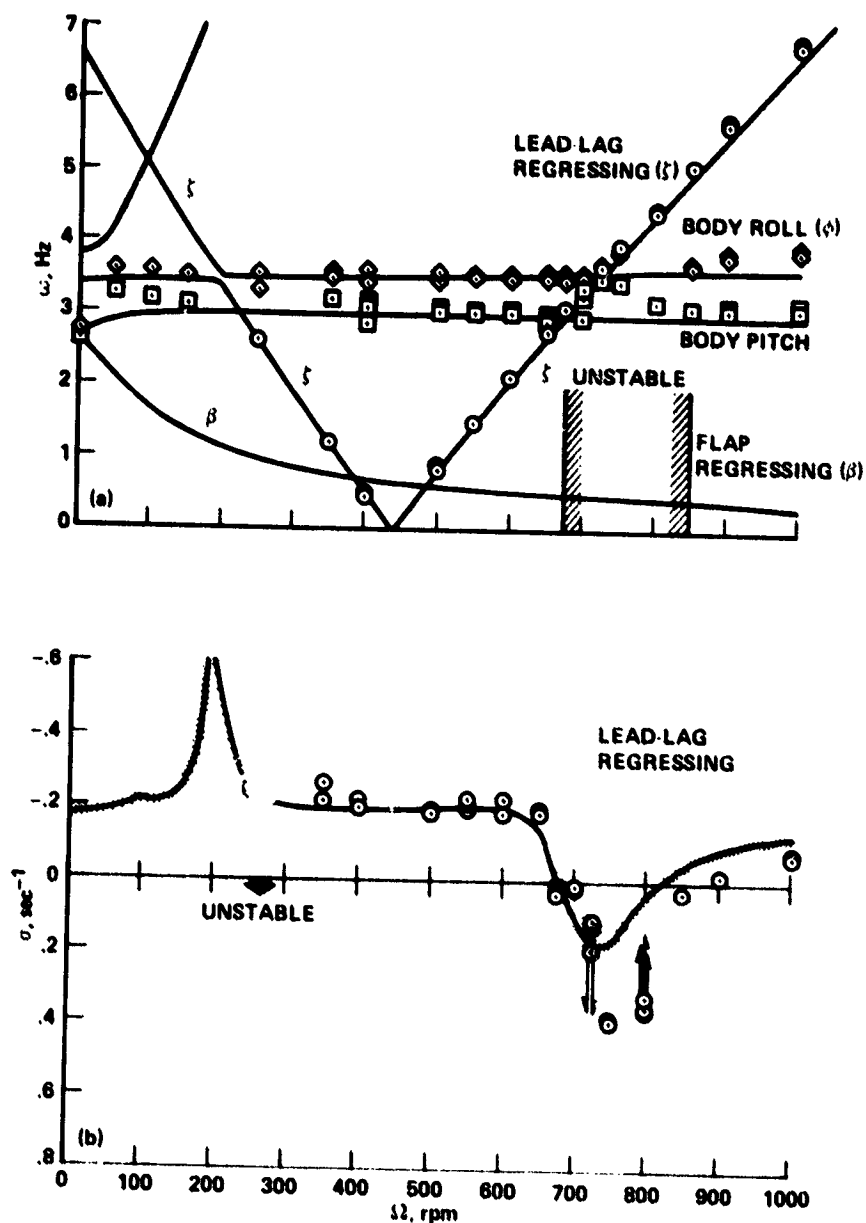
Figure 14.- Tantalum stub blades with pitch and roll freedom; $\omega_{\theta 0} = 2.58 \text{ Hz}$, $\omega_{\phi 0} = 2.55 \text{ Hz}$.



(a) Modal frequency.

(b) Lead-lag regressing mode damping (shaded area shows effect of doubling and halving nominal body damping).

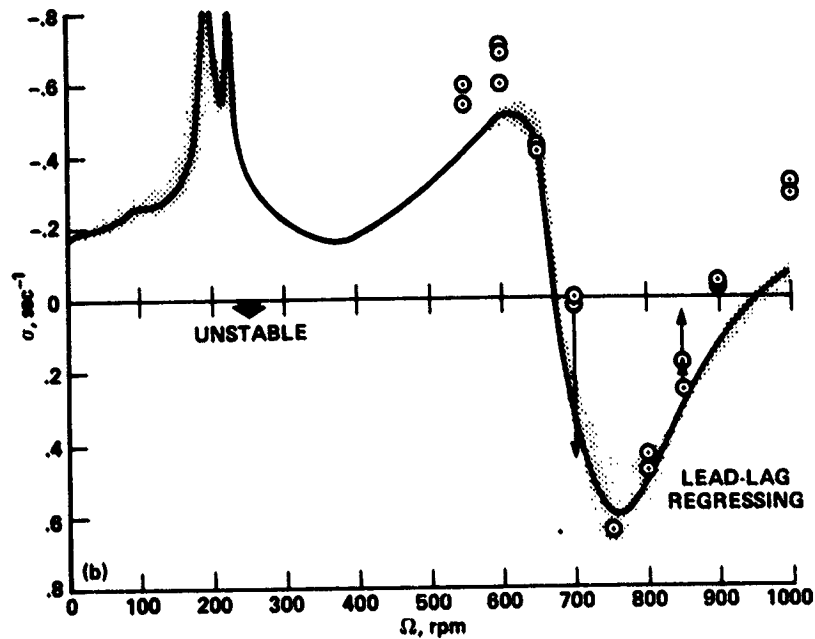
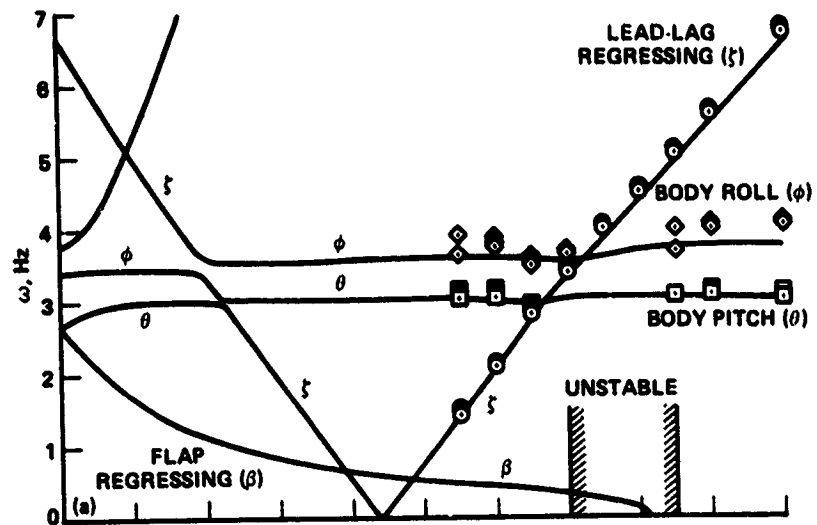
Figure 15.- Aerodynamic blades with roll freedom; $\omega_{\phi 0} = 2.79$ Hz, $\theta_b = 0^\circ$.



(a) Modal frequency.

(b) Lead-lag regressing mode damping (shaded area shows effect of doubling and halving nominal body damping).

Figure 16.- Aerodynamic blades with pitch and roll freedom; $\omega_{\phi 0} = 2.62$ Hz, $\omega_{\phi 0} = 2.73$ Hz, $\theta_b = 0^\circ$.



(a) Modal frequency.

(b) Lead-lag regressing mode damping (shaded area shows effect of doubling and halving nominal body damping).

Figure 17.- Aerodynamic blades with pitch and roll freedom; $\omega_{\theta 0} = 2.62$ Hz,
 $\omega_{\phi 0} = 2.73$ Hz, $\theta_b = 8.9^\circ$.

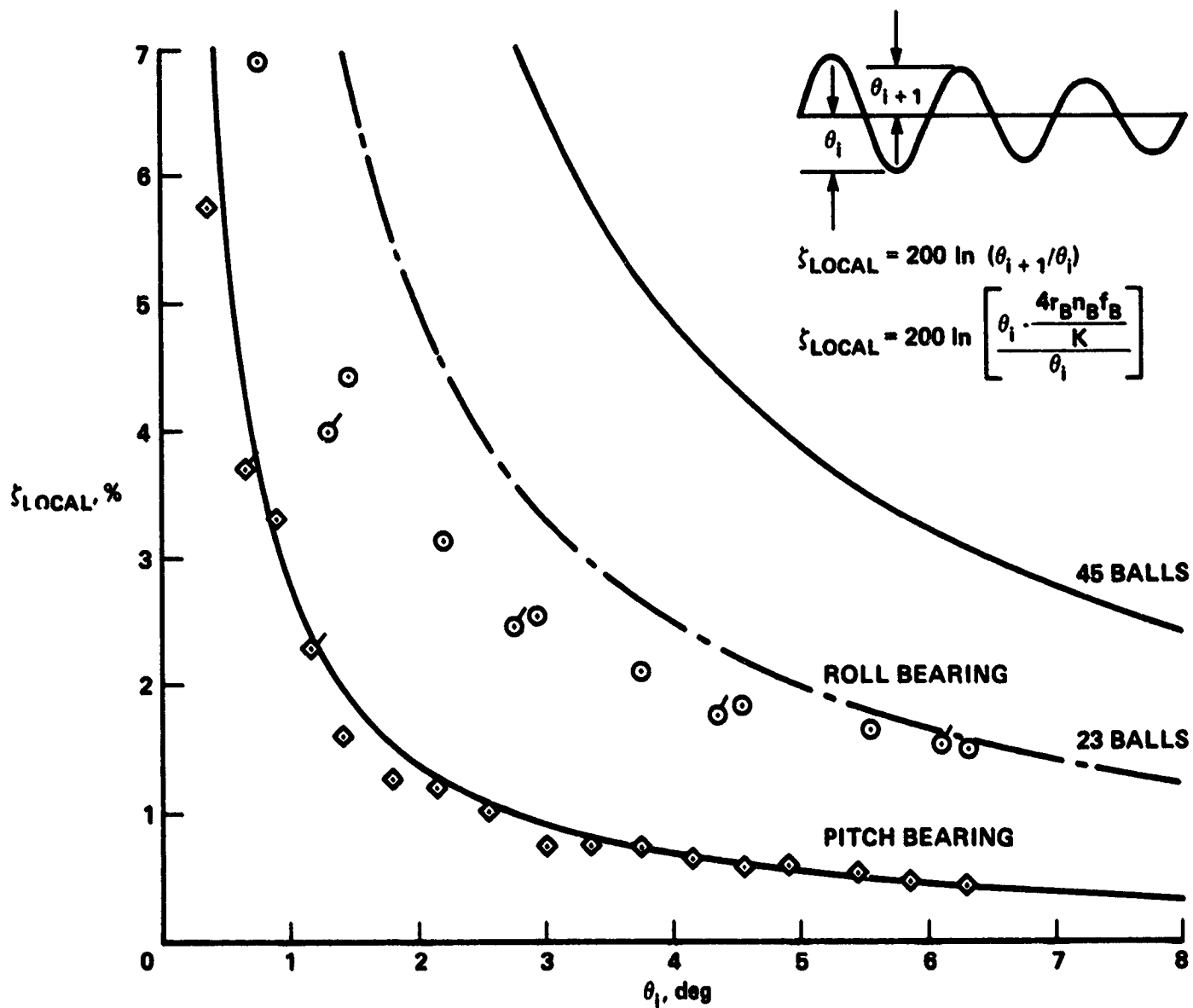


Figure 18.- Local damping coefficient of gimbal pitch and roll bearings; flagged symbols are repeat points.

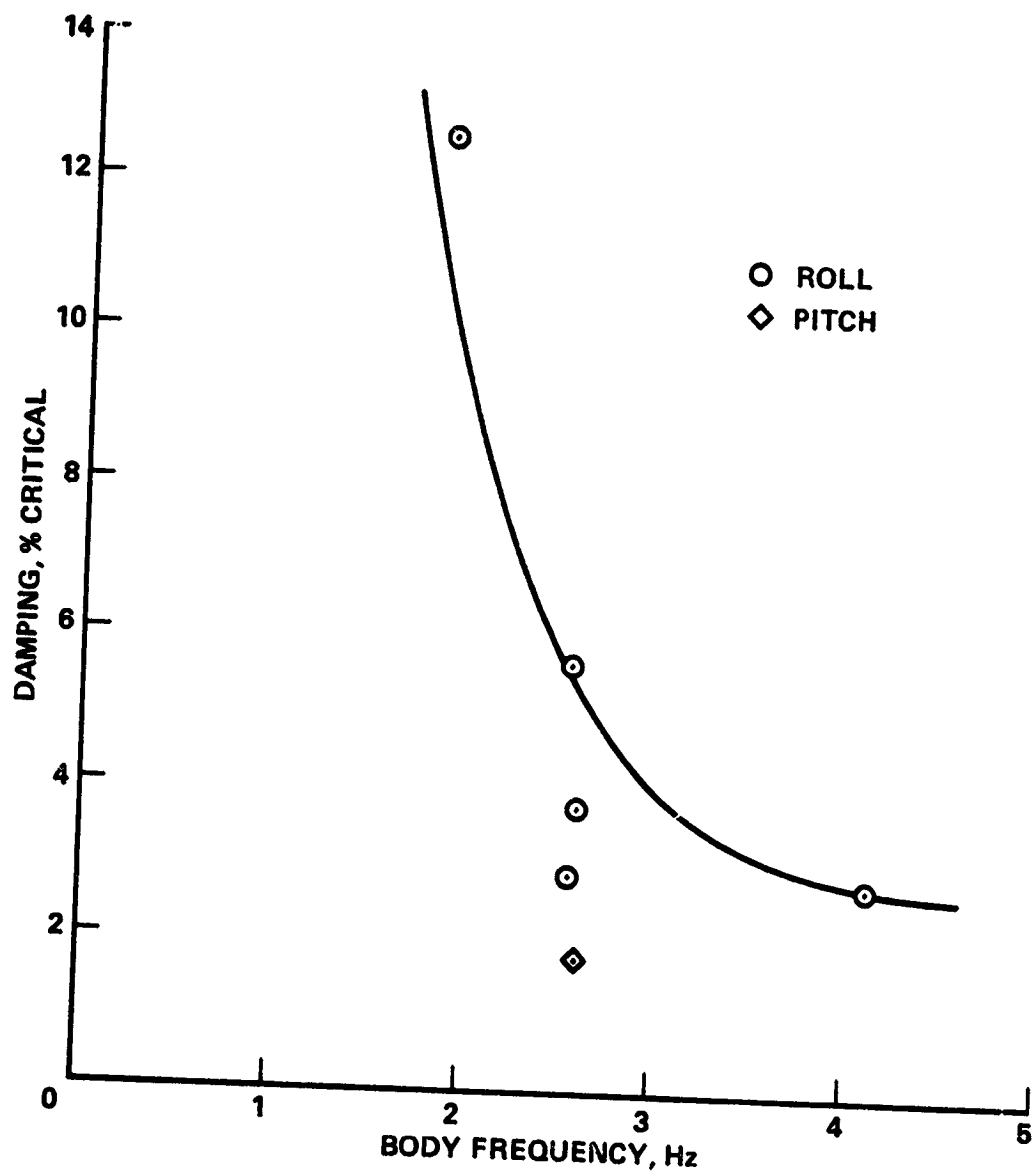


Figure 19.- Nonrotating body damping for tantalum stub blade configurations.

1. Report No. NASA TM-78489 AVRADCOM Tech. Rep. 78-17(AM)		2. Government Accession No.		3. Recipient's Catalog No.	
4. Title and Subtitle AN EXPERIMENTAL INVESTIGATION OF HINGELESS HELICOPTER ROTOR-BODY STABILITY IN HOVER				5. Report Date	
				6. Performing Organization Code	
7. Author(s) William G. Bousman				8. Performing Organization Report No. A-7430	
9. Performing Organization Name and Address Ames Research Center, NASA, and AVRADCOM Research and Technology Laboratories Moffett Field, Calif. 94038				10. Work Unit No. 992-21-01	
				11. Contract or Grant No.	
12. Sponsoring Agency Name and Address National Aeronautics and Space Administration Washington, D.C. 20546 and U.S. Army Aviation Research and Development Command St. Louis, MO 93166				13. Type of Report and Period Covered Technical Memorandum	
				14. Sponsoring Agency Code	
15. Supplementary Notes					
16. Abstract Model tests of a 1.62-m diameter rotor were performed to investigate the aeromechanical stability of coupled rotor-body systems in hover. Experimental measurements were made of modal frequencies and damping over a wide range of rotor speeds. Good data were obtained for the frequencies of the rotor lead-lag regressing, body pitch and body roll mode, and the damping of the lead-lag regressing mode. The quality of the damping measurements of the body modes was poor due to nonlinear damping in the gimbal ball bearings. Simulated vacuum testing was performed using substitute blades of tantalum that reduced the effective Lock number to 0.2% of the model scale value while keeping the blade inertia constant. The experimental data were compared with theoretical predictions, and the correlation was in general very good.					
17. Key Words (Suggested by Author(s)) Hingeless rotor stability Air resonance Ground resonance			18. Distribution Statement Unlimited STAR Category - 01		
19. Security Classif. (of this report) Unclassified		20. Security Classif. (of this page) Unclassified		21. No. of Pages 47	
				22. Price* \$4.00	